Interface-preserving level set method for simulating dam-break flows

Z.H. Gu [a], H.L. Wen [b], C.H. Yu [c,*], Tony W.H. Sheu [b,d,e]

[a] College of Civil Engineering and Architecture, Zhejiang University, Hangzhou, People's Republic of China
[b] Department of Engineering Science and Ocean Engineering, National Taiwan University, Taiwan, Republic of China
[c] State Key Lab. of Hydraulics and Mountain River Engineering, Sichuan University, Sichuan 610065, People's Republic of China
[d] Institute of Applied Mathematical Sciences, National Taiwan University, Taiwan, Republic of China
[e] Center for Advanced Study in Theoretical Sciences, National Taiwan University, Taiwan, Republic of China

ARTICLE INFO

ABSTRACT

An interface-preserving level set method that solves advection and re-initialization equations for simulating three-dimensional dam-break flows is developed. This method solves mass transfer problems on a uniform staggered Cartesian grid. The advection equation that is used to advect the level set function for capturing the interface is discretized by a proposed fourth-order spatial discretization scheme. This scheme is dispersion-relation-preserving and is compact-reconstruction weighted essentially non-oscillatory (DRP-CRWENO4). This scheme is compared with a previous fifth-order, weighted, essentially non-oscillatory (WENO5) scheme and can represent an interface more accurately, while exactly preserving mass conservation. This level set approach introduces a mass correction term into the re-initialization equation based on local interface-preserving conditions. An explicit Adams–Bashforth algorithm on a staggered Eulerian grid is used for the Navier–Stokes solver. The point successive over-relaxation method is then employed to solve the resulting linear system. Two one-dimensional wave propagation problems are simulated to verify the proposed DRP-CRWENO4 scheme, which is shown to be capable of effectively capturing large gradients with fourth-order accuracy. To demonstrate their resolution, the two advection schemes (WENO5 and DRP-CRWENO4) are applied in two two-dimensional benchmark cases, i.e., a vortex deforming problem and Zalesak's disk problem, where simulation results of both schemes are compared against each other. Demonstration study is then further extended to three-dimensional cases of the vortex deforming problem and Zalesak's sphere problem, and simulation results agree well with those using hybrid particle level set method. Finally, several dam-break problems with and without obstacles are investigated to validate the coupled two-phase incompressible flow and level set method solver. The results for the predicted flow structure and mass conservation properties are compared with the reported experimental data or numerical simulations.

© 2018 Elsevier Inc. All rights reserved.

* Corresponding author.
   E-mail address: chyu@zju.edu.cn (C.H. Yu).

1. Introduction

Dams provide benefits, including flood protection, power generation, and irrigation. A dam-break accident can cause significant losses of life and property, as well as environmental damage [1]. Dam-break flow is a high-density-ratio fluid, and its interface is usually subject to large and complex deformations by transient convection-dominated processes. An efficient numerical scheme should both accurately predict the position of the interface and maintain mass conservation for the dam-break flow [2]. The focus of this paper is to develop a high-resolution scheme to capture the interface accurately, so that mass is conserved as much as possible. Once mass conservation is well satisfied, the water height and surge front location for the dam-break flow can be better solved naturally.

To treat gas/liquid interface in incompressible flow, a novel approach is proposed [3]. In their approach, the problem is reformulated monolithically to avoid stability issues induced by partitioned methods for solid-fluid coupling. This approach has been shown to be quite robust and effective on more realistic problems including those with multiple bubbles, merging and pinching, etc. Over the last decade, the level set method has become popular for simulating gas/liquid two-phase flows because of its advantages [4–11]. One of its advantages is that the interface in a level set method is defined by the zero contour of a continuous signed distance function. Thus, its normality and curvature can be easily calculated. Additionally, the level set method handles topology changes relatively easily by implementing a high-order advection scheme, such as a finite volume or finite difference scheme [12]. However, existing level set methods are typically plagued by two key issues. First, because of numerical dissipation and dispersion, discretization schemes cause deterioration in predicted level set solutions. Second, a re-initialization procedure is required to maintain the level set function as a signed distance function. A disadvantage of this method is that a small amount of mass may be gained or lost when the zero level set is altered [13].

Solutions near the zero-level set are discretized using weighted essentially non-oscillatory (WENO) schemes. This type of structured adaptive mesh refinement technique was used in [14]. The level set solutions were also calculated in [15] using a high-order WENO scheme on a separate equidistant refined Cartesian grid. Salih et al. [16] studied the MacCormack method, the second-order essentially non-oscillatory (ENO) scheme, the fifth-order WENO scheme, and high-order schemes to investigate the accuracy of the advection process for the level set equation. They demonstrated that the high-order schemes can preserve interface shape and exactly conserve the mass properties of fluids. In the above references, high-order discretization schemes were shown to solve level set equations, and were capable of yielding accurate solutions.

In order to reduce mass loss, a re-initialization step is suggested for improving the process. In 1997, Sussman and Fatemi corrected the mass property by adding an additional mass correction term to the re-initialization equation [17]. This correction conserves the mass bounded by the interface and maintains the level set function as a distance function. In [18], Ni et al. proposed a variable time-step level set method to improve conservation. A re-initialization procedure for solving the perturbed Hamilton–Jacobi equation was studied by Chang et al. [19] to show the mass conservation. Instead of solving the re-initialization equation, a conservative level set method that solves the artificial compression–diffusion equation using a smoothed Heaviside function (rather than a distance function) was developed in [20–22]. A geometric mass-preserving re-distancing scheme [23] and volume re-initialization scheme [24] involving the effects of local curvature have been proposed to resolve the problems associated with the re-initialization step. Recently, Shao et al. took a mass remedy procedure based on local curvature at the interface into account in their discussion of mass conservation properties [13].

Another important technique for improving mass conservation in level set methods is to adopt a hybrid approach, namely a coupled level set/volume-of-fluid (CLSVOF) method. This method benefits from both the smoothed interface description of the level set method and the good mass conservation properties of the volume-of-fluid (VOF) approach [25–30]. Taking the advantages of the VOF and level set methods into account, a coupled VOF and level set (VOSET) method has been developed to calculate incompressible two-phase flows [31–33]. The major issue in this hybrid method is that the level set function is calculated by an iterative geometric approach to resolve the physically sharp interface without incurring contact discontinuous oscillations [31]. Recently, the VOSET method aims to build a more comprehensive understanding of incompressible two-phase flow in unstructured triangular grids [34]. An additional hybrid approach using level sets and volume fractions without the need for complicated interface construction is worthy of further investigation [35,36].

In contrast to the aforementioned level set methods, the hybrid particle level set (HPLS) method uses Lagrangian markers to correct the front location predicted by Eulerian transport [37]. This method is useful in addressing a large variety of problems including simulation of rigid body rotation of Zalesak's disk, deformation of circular bubbles and two/three-dimensional deformation field that involves moving interface. Following the pioneering work of Enright et al. [37], Ref. [38] proposes a new non-overlapping concept which is implemented in the reseeding procedure of HPLS method in order to maintain resolution of the surface during runtime. Refs. [39–41] using improved particle level set methods to model complex two-phase flows also produce satisfactory results.

In the present study, we develop an accurate fourth-order dispersion-relation-preserving, compact reconstruction weighted essentially non-oscillatory (DRP-CRWENO4) scheme for capturing an interface on a uniform staggered Cartesian grid. This compact scheme, which accommodates better dispersion relation and avoids numerical oscillation by using a non-oscillatory limiter for the advective terms in the level set equation, is developed using a three compact grid stencil. Additionally, the interface-preserving level set method proposed by Ref. [17] is adopted to conserve mass bounded by the interface by adding a mass correction term. This article is organized as follows. In Section 2, governing equations are presented for the two fluids and the two-step interface preserving level set method. Section 3 describes the proposed solution

algorithm and high-resolution DRP-CRWENO4 scheme that can resolve solution accuracy and improve mass conservation. In Section 4, the employed analysis code is verified. It is used to solve a one-dimensional wave equation with a sharp and discontinuous initial condition, and two pure advection examples (Zalesak's disk and a vortex deforming problem). Some numerical results for dam-break flows with/without obstacles, solved using the Adams–Bashforth algorithm, are presented in Section 5. Section 6 presents the conclusion.

2. Mathematical model

2.1. Interface-preserving level set method

The level set function ϕ set as a signed distance function $\bar{d}$ is defined to be positive for liquid, negative for gas, with the interface level located at zero ψ:

$$\phi(x, t = 0) = \begin{cases} \bar{d}; & \text{for } x \text{ in the liquid} \\ 0; & \text{for } x \in \psi \\ -\bar{d}; & \text{for } x \text{ in the gas.} \end{cases} \tag{1}$$

The motion of the interface can be tracked by solving the following level set evolution equation:

$$\phi_t + \mathbf{u} \cdot \nabla \phi = 0. \tag{2}$$

As time progresses, the level set function ϕ is no longer the signed distance function. It is necessary to keep ϕ as a signed distance function because the density and viscosity are incorporated near the interface. For this reason, a re-initialization step that solves the following equation to a steady state is employed [42]:

$$\phi_\tau + \bar{S}(\phi_0)(|\nabla \phi| - 1) = 0, \tag{3}$$

where τ is the pseudo-time for the iteration and ϕ_0 is the level set function before re-initialization (i.e., $\phi_0(\mathbf{x}) = \phi(\mathbf{x}, \tau = 0)$). Note that $\bar{S}(\phi_0)$ denotes the smoothed sign function, with Δx being the local grid size

$$\bar{S}(\phi_0) = 2\left(\bar{H}(\phi_0) - 0.5\right), \tag{4}$$

with

$$\bar{H}(\phi) = \begin{cases} 0; & \text{if } \phi < -\varepsilon \\ \frac{1}{2}[1 + \frac{\phi}{\varepsilon} + \frac{1}{\pi}\sin(\frac{\pi\phi}{\varepsilon})]; & \text{if } |\phi| \leq \varepsilon \\ 1; & \text{if } \phi > \varepsilon, \end{cases} \tag{5}$$

where $\varepsilon = 1.5\Delta x$ and Δx indicates the grid spacing. In the numerical computations, the position of the interface will change. Because of this moving interface, small mass errors can accumulate and the overall error can become very large. To overcome this problem, the volume of the domain can be conserved using a modified re-initialization equation:

$$\phi_\tau = \bar{S}(\phi_0)(1 - |\nabla \phi|) + \lambda \delta(\phi)|\nabla \phi|, \tag{6}$$

with

$$\lambda = -\frac{\int_\Omega \delta(\phi)(\bar{S}(\phi_0)(1 - |\nabla \phi|))d\Omega}{\int_\Omega \delta^2(\phi)|\nabla \phi|d\Omega}, \tag{7}$$

where the delta function $\delta(\phi)$ is given as

$$\delta(\phi) = \begin{cases} \frac{1}{2\varepsilon}(1 + \cos(\frac{\pi\phi}{\varepsilon})); & \text{if } |\phi| \leq \varepsilon; \\ 0; & \text{otherwise.} \end{cases} \tag{8}$$

Equations (2) and (6) constitute the working set of the interface-preserving level set method [17].

2.2. Navier–Stokes equations and physical properties

The two immiscible incompressible fluids are expressed by the Navier–Stokes equations:

$$\nabla \cdot \mathbf{u} = 0, \tag{9}$$

$$\frac{\partial \mathbf{u}}{\partial t} + \mathbf{u} \cdot \nabla \mathbf{u} = -\frac{1}{\rho}\nabla p + \frac{1}{\rho}\nabla \cdot [\mu(\nabla \mathbf{u} + (\nabla \mathbf{u})^T)] + \mathbf{g}, \tag{10}$$

where **u** is the velocity, p the pressure, and **g** the gravitational acceleration. To avoid numerical instability at the interface (particularly for large density ratios of gas and liquid), a physical property across the thickness of the diffused interface is adopted that varies smoothly from gas to fluid. The density and viscosity in Eq. (10) can be expressed as

$$\rho(\phi) = \rho_G + (\rho_L - \rho_G)\bar{H}(\phi),$$
$$\mu(\phi) = \mu_G + (\mu_L - \mu_G)\bar{H}(\phi),$$

(11)

where the subscripts G and L represent the gas and liquid phases, respectively. It is noted that the Ghost Fluid Method (GFM) is a method proposed by Fedkiw et al. [43] combining the best properties of Eulerian and Lagrangian schemes while avoiding their shortcomings at the same time [43]. In their GFM, a level set function is used to track the motion of a multimaterial interface in an Eulerian framework, and a Heaviside profile of the density with no numerical smearing is maintained by use of ghost cells. In the near future, the ghost fluid method will be adopted because of its advantages and will be further applied for the air bubble or water droplet problems where surface tension is taken into consideration.

3. Numerical scheme

Dam-break flows are investigated numerically in this study using a finite difference scheme in a uniform staggered Cartesian grid. For the staggered arrangement of the variables, the velocity components u, v, and w are located at the centers of cell faces in the x, y, and z directions, respectively. ρ, μ, p, and ϕ are defined at the cell centers.

3.1. Level set method solver

The DRP upwinding compact difference scheme proposed in section 3.1.1.1 and the DRP-CRWENO4 scheme proposed in section 3.1.1.2 are primarily this paper's original work, which have never appeared in any existing literature. The WENO5 discretization scheme adopted in section 3.1.2 is proposed by Ref. [49].

3.1.1. Approximation of spatial derivatives for the level set evolution equation

The level set evolution equation (i.e., Eq. (2)) can be expressed in its conservation form, because **u** is divergence-free

$$\phi_t + \nabla \cdot (\mathbf{u}\phi) = 0.$$

(12)

Using a uniform grid in one space dimension as an example, Eq. (12) results in an ordinary differential equation (ODE) with a semi-discrete conservative finite difference scheme

$$\frac{d\phi_i}{dt} = L(u_i) = -\frac{1}{\Delta x}(\hat{F}_{i+\frac{1}{2}} - \hat{F}_{i-\frac{1}{2}}).$$

(13)

The approximation of numerical flux $\hat{F}_{i+\frac{1}{2}}$ at point $x_{i+\frac{1}{2}}$ can be reconstructed from the discrete values of $F = \phi u$. The motivation of DRP-CRWENO4 scheme to approximate numerical flux is as follows. First, we construct a dispersion-relation-preserving (DRP) upwinding compact difference scheme to approximate first derivative terms with higher accuracy, less dispersion and dissipation errors in smooth regions. This scheme is constructed based on three weighted compact interpolations. Following this, numerical oscillations are avoided near discontinuities by optimizing the weighting factors based on the WENO theory. Less numerical dissipation errors are observed near discontinuities because of the compact interpolation schemes adopted. Therefore, the DRP-CRWENO4 proposed in this paper achieves fourth-order accuracy in smooth regions with less dispersion and dissipation errors and avoids oscillations near discontinuities when discretizing first order derivatives.

3.1.1.1. DRP upwinding compact difference scheme   Finite difference schemes encounter two primary problems: numerical dissipation and numerical dispersion errors. Classical numerical schemes such as MacCormack schemes, upwind schemes, and ENO schemes have been found to be unsatisfactory for wave propagation studies, especially over long distances and large time intervals [44]. To improve the resolution of classical numerical schemes, Lele [45] developed a center-type compact difference scheme, by imposing the modified wavenumber to be equal to the exact wavenumber at certain nodal points. Unfortunately, the lack of numerical dissipation may cause spurious numerical oscillations in practical applications. Tam and Webb [46] proposed center-type dispersion-relation-preserving (DRP) finite difference schemes that minimize integrated errors over the range of the wavenumber. A center-type DRP scheme can minimize numerical dispersion errors and produces no dissipation errors. To improve a center-type compact difference scheme for nonlinear convective terms, an optimized third-order upwind compact scheme is validated by solving time-dependent nature convection problems [47].

In this study, to accurately solve the level set equation over a longer simulation time, a DRP upwind compact difference scheme with lower dispersion errors is developed for approximating first derivative terms. We design an upwind compact difference scheme using the following formula

$$\overline{A}\frac{\partial F}{\partial x}|_{i-1} + \frac{\partial F}{\partial x}|_i + \overline{C}\frac{\partial F}{\partial x}|_{i+1} = \frac{\overline{a}F_{i-2} + \overline{b}F_{i-1} + \overline{c}F_i + \overline{d}F_{i+1}}{\Delta x}.$$

(14)

Using Taylor series expansions for the terms $\frac{\partial F}{\partial x}|_{i-1}$, $\frac{\partial F}{\partial x}|_{i+1}$, F_{i-2}, F_{i-1}, and F_{i+1} with respect to F_i, the leading six truncation error terms can be eliminated in the modified equation. The following set of algebraic equations are obtained:

$$\bar{a} + \bar{b} + \bar{c} + \bar{d} = 0, \tag{15}$$

$$-2\bar{a} - \bar{b} + \bar{d} - \bar{A} - \bar{C} = 1, \tag{16}$$

$$2\bar{a} + \frac{1}{2}\bar{b} + \frac{1}{2}\bar{d} + \bar{A} - \bar{C} = 0, \tag{17}$$

$$-\frac{4}{3}\bar{a} - \frac{1}{6}\bar{b} + \frac{1}{6}\bar{d} - \frac{1}{2}\bar{A} - \frac{1}{2}\bar{C} = 0, \tag{18}$$

$$\frac{2}{3}\bar{a} + \frac{1}{24}\bar{b} + \frac{1}{24}\bar{d} + \frac{1}{6}\bar{A} - \frac{1}{6}\bar{C} = 0, \tag{19}$$

$$-\frac{4}{15}\bar{a} - \frac{1}{120}\bar{b} + \frac{1}{120}\bar{d} - \frac{1}{24}\bar{A} - \frac{1}{24}\bar{C} = 0. \tag{20}$$

The coefficients from the above formulas can be derived as follows: $\bar{A} = \frac{1}{2}$, $\bar{C} = \frac{1}{6}$, $\bar{a} = -\frac{1}{18}$, $\bar{b} = -1$, $\bar{c} = \frac{1}{2}$, and $\bar{d} = \frac{5}{9}$. These derived coefficients can be applied to get the fifth-order spatial accuracy of the first-order derivative term

$$\frac{\partial F}{\partial x} = \frac{\partial F}{\partial x}|_{exact} + \frac{1}{60}\Delta x^5 \frac{\partial^6 F}{\partial x^6} + O(\Delta x^6). \tag{21}$$

Optimized coefficients can also be derived as shown in Eq. (14) by using the DRP finite difference approximation of the first derivative $\frac{\partial F}{\partial x}$ in wavenumber space [46]. In other words, an excellent match between the exact wavenumber and numerical wavenumber is obtained by reducing the dispersion error for the approximated first-order derivative term. We perform a modified number approach [46] on each term shown in Eq. (14)

$$\mathbf{i}\alpha'\Delta x(\bar{A}\mathbf{e}^{-\mathbf{i}\alpha\Delta x} + 1 + \bar{C}\mathbf{e}^{\mathbf{i}\alpha\Delta x}) = \bar{a}\mathbf{e}^{-2\mathbf{i}\alpha\Delta x} + \bar{b}\mathbf{e}^{-\mathbf{i}\alpha\Delta x} + \bar{c} + \bar{d}\mathbf{e}^{\mathbf{i}\alpha.\Delta x}. \tag{22}$$

Therefore, the numerical wavenumber $\alpha'\Delta x$ can be written as

$$\alpha'\Delta x = \frac{\mathbf{i}(-3\mathbf{e}^{-2\mathbf{i}\alpha\Delta x} + 4\mathbf{e}^{-2\mathbf{i}\alpha\Delta x}\overline{d} - 24\mathbf{e}^{-\mathbf{i}\alpha\Delta x} + 18\mathbf{e}^{-\mathbf{i}\alpha\Delta x}\overline{d} + 27 - 36\overline{d} + 14\overline{d}\mathbf{e}^{\mathbf{i}\alpha\Delta x})}{-14 - 17\mathbf{e}^{-\mathbf{i}\alpha\Delta x} + 18\mathbf{e}^{-\mathbf{i}\alpha\Delta x}\overline{d} + \mathbf{e}^{\mathbf{i}\alpha\Delta x} - 6\overline{d}\mathbf{e}^{\mathbf{i}\alpha\Delta x}}. \tag{23}$$

In order to obtain a better dispersion accuracy for α', it is required that $\alpha\Delta x \approx \Re[\alpha'\Delta x]$, where $\Re[\alpha'\Delta x]$ is the real part of $\alpha'\Delta x$, which implies that $E(\alpha)$ defined below should be small and positive

$$E(\alpha) = \int\limits_0^{\frac{17\pi}{20}} \left[W \cdot \left(\alpha\,\Delta x - \Re[\alpha'\,\Delta x] \right) \right]^2 d(\alpha\Delta x). \tag{24}$$

It should be noted that Eq. (24) can be analytically integrable if the weighting function W shown above is the denominator of $(\alpha\Delta x - \Re[\alpha'\Delta x])$. The following condition is enforced to ensure that E defined in Eq. (24) is positive and minimum

$$\frac{\partial E}{\partial \overline{d}} = 0. \tag{25}$$

Note that the integration range rendering the smallest value of E is numerically determined from several ranges by MAPLE software (in this study we choose $0 \leq \alpha\Delta x \leq \frac{17\pi}{20}$). Equation (25) and five other algebraic equations shown in (15)–(19) are used to obtain the optimized coefficients: $\bar{A} = 0.5418416108$, $\bar{C} = 0.1527194630$, $\bar{a} = -0.0648536914$, $\bar{b} = -1.041841611$, $\bar{c} = 0.583683223$, and $\bar{d} = 0.5230120803$. The fourth-order spatial accuracy of the first-order derivative term can be obtained by using above optimized coefficients

$$\frac{\partial F}{\partial x} = \frac{\partial F}{\partial x}|_{exact} + 0.00139472\,\Delta x^4 \frac{\partial^5 F}{\partial x^5} + O(\Delta x^5). \tag{26}$$

It can be seen from the truncation errors of Eq. (21) and Eq. (26) that the accuracy of this compact difference scheme has changed from fifth order to fourth order.

A high-order compact interpolation was proposed by Lele [45]. In that equation, physical values for the cell faces can be interpolated from the physical values for the cell centers. The equation takes the following form: Define the values of $\hat{F}$ at the half nodal points as follows

$$\widetilde{A}\hat{F}_{i-\frac{1}{2}} + \hat{F}_{i+\frac{1}{2}} + \widetilde{C}\hat{F}_{i+\frac{3}{2}} = \widetilde{a}F_{i-1} + \widetilde{b}F_i + \widetilde{c}F_{i+1}, \tag{27}$$

and

$$\widetilde{A}\hat{F}_{i-\frac{3}{2}} + \hat{F}_{i-\frac{1}{2}} + \widetilde{C}\hat{F}_{i+\frac{1}{2}} = \widetilde{a}F_{i-2} + \widetilde{b}F_{i-1} + \widetilde{c}F_i. \tag{28}$$

The coefficients in Eq. (27) and Eq. (28), which are $\widetilde{A} = 0.5418416108$, $\widetilde{C} = 0.1527194630$, $\widetilde{a} = 0.0648536914$, $\widetilde{b} = 1.106695303$, and $\widetilde{c} = 0.5230120803$, have been derived by comparing the optimized coefficients derived in Eq. (14) for $\frac{\partial F}{\partial x} = \frac{\hat{F}_{i+\frac{1}{2}} - \hat{F}_{i-\frac{1}{2}}}{\Delta x}$. We provide a detailed calculation for these coefficients in Appendix.

3.1.1.2. DRP-CRWENO4 scheme Discontinuous solutions may occur for the level set evolution equations even if numerical dispersion errors are reduced. The DRP-CRWENO4 scheme, which achieves high-order accuracy with low dispersion errors in smooth regions and uses compact stencils near discontinuities to avoid oscillations, is developed to approximate the convective flux term $\frac{\partial F}{\partial x}$. Numerical flux at the cell faces can also be approximated by the following three third-order compact interpolations [48]

$$\frac{2}{3}\hat{F}_{i-\frac{1}{2}} + \frac{1}{3}\hat{F}_{i+\frac{1}{2}} = \frac{1}{6}(F_{i-1} + 5F_i), \tag{29}$$

$$\frac{1}{3}\hat{F}_{i-\frac{1}{2}} + \frac{2}{3}\hat{F}_{i+\frac{1}{2}} = \frac{1}{6}(5F_i + F_{i+1}), \tag{30}$$

$$\frac{2}{3}\hat{F}_{i+\frac{1}{2}} + \frac{1}{3}\hat{F}_{i+\frac{3}{2}} = \frac{1}{6}(F_i + 5F_{i+1}). \tag{31}$$

The new numerical flux at the half nodal points is a combination of the above three third-order compact interpolations that are sequentially multiplied by coefficients c_i for $i = 1$–3:

$$\left[\frac{2c_1 + c_2}{3}\right]\hat{F}_{i-\frac{1}{2}} + \left[\frac{c_1 + 2(c_2 + c_3)}{3}\right]\hat{F}_{i+\frac{1}{2}} + \frac{c_3}{3}\hat{F}_{i+\frac{3}{2}}$$
$$= \frac{c_1}{6}F_{i-1} + \left[\frac{5(c_1 + c_2) + c_3}{6}\right]F_i + \left[\frac{c_2 + 5c_3}{6}\right]F_{i+1}. \tag{32}$$

After a term-by-term comparison of the coefficients for Eq. (27) and Eq. (32), we can obtain the coefficients $c_1 = 0.20891$, $c_2 = 0.5$, and $c_3 = 0.29109$.

Based on the idea of a WENO scheme [44], the numerical fluxes at cell faces that are reconstructed using a left-biased interpolation can be rewritten in the form of Eq. (32)

$$\left[\frac{2\omega_1 + \omega_2}{3}\right]\hat{F}^L_{i-\frac{1}{2}} + \left[\frac{\omega_1 + 2(\omega_2 + \omega_3)}{3}\right]\hat{F}^L_{i+\frac{1}{2}} + \frac{\omega_3}{3}\hat{F}^L_{i+\frac{3}{2}}$$
$$= \frac{\omega_1}{6}F_{i-1} + \left[\frac{5(\omega_1 + \omega_2) + \omega_3}{6}\right]F_i + \left[\frac{\omega_2 + 5\omega_3}{6}\right]F_{i+1}. \tag{33}$$

The weighting factors ω_k in Eq. (33) are defined as

$$\omega_k = \frac{\alpha_k}{\sum_k \alpha_k}, \quad k = 1, 2, 3, \tag{34}$$

with

$$\alpha_k = c_k\left(1 + \frac{|\beta_3 - \beta_1|}{\epsilon + \beta_k}\right), \quad k = 1, 2, 3. \tag{35}$$

We set ϵ as 10^{-6} in this study to avoid the denominator becoming zero. The following smoothness indicators β_k imply the smoothness of the numerical flux for a stencil in the solution:

$$\beta_k = \sum_{l=1}^{2} \int_{x_{i-1/1}}^{x_{i+1/2}} \Delta x^{2l-1}(\frac{\partial^l p_k(x)}{\partial^l x})^2 dx, \; k = 1, 2, 3, \tag{36}$$

where $p_k(x)$ is the second-order polynomial constructed over the interval $[x_{i-1/2}, x_{i+1/2}]$ [44]. For $k = 1, 2, 3$, Eq. (36) amounts to

$$\beta_1 = \frac{13}{12}(F_{i-2} - 2F_{i-1} + F_i)^2 + \frac{1}{4}(F_{i-2} - 4F_{i-1} + 3F_i)^2,$$

$$\beta_2 = \frac{13}{12}(F_{i-1} - 2F_i + F_{i+1})^2 + \frac{1}{4}(F_{i-1} - F_{i+1})^2, \tag{37}$$

$$\beta_3 = \frac{13}{12}(F_i - 2F_{i+1} + F_{i+2})^2 + \frac{1}{4}(3F_i - 4F_{i+1} + F_{i+2})^2.$$

Similarly, the DRP-CRWENO4 scheme for the right-biased interpolation can be expressed as

$$\left[\frac{2\widetilde{\omega}_1 + \widetilde{\omega}_2}{3}\right]\hat{F}^R_{i+\frac{3}{2}} + \left[\frac{\widetilde{\omega}_1 + 2(\widetilde{\omega}_2 + \widetilde{\omega}_3)}{3}\right]\hat{F}^R_{i+\frac{1}{2}} + \frac{\widetilde{\omega}_3}{3}\hat{F}^R_{i-\frac{1}{2}} \tag{38}$$

$$= \frac{\widetilde{\omega}_1}{6}F_{i+2} + \left[\frac{5(\widetilde{\omega}_1 + \widetilde{\omega}_2) + \widetilde{\omega}_3}{6}\right]F_{i+1} + \left[\frac{\widetilde{\omega}_2 + 5\widetilde{\omega}_3}{6}\right]F_i,$$

where

$$\widetilde{\omega}_k = \frac{\widetilde{\alpha}_k}{\sum_k \widetilde{\alpha}_k}, \quad \widetilde{\alpha}_k = c_k\left(1 + \frac{|\widetilde{\beta}_3 - \widetilde{\beta}_1|}{\epsilon + \widetilde{\beta}_k}\right), \quad k = 1, 2, 3, \tag{39}$$

and

$$\widetilde{\beta}_1 = \frac{13}{12}(F_{i+1} - 2F_{i+2} + F_{i+3})^2 + \frac{1}{4}(3F_{i+1} - 4F_{i+2} + F_{i+3})^2,$$

$$\widetilde{\beta}_2 = \frac{13}{12}(F_i - 2F_{i+1} + F_{i+2})^2 + \frac{1}{4}(F_i - F_{i+2})^2, \tag{40}$$

$$\widetilde{\beta}_3 = \frac{13}{12}(F_{i-1} - 2F_i + F_{i+1})^2 + \frac{1}{4}(F_{i-1} - 4F_i + 3F_{i+1})^2.$$

In summary, numerical flux can be reconstructed using left and right-biased interpolation to approximate first derivative terms based on the sign of the wave speed. In the framework of flux-splitting method [49], the flux is the combination of right and left-side fluxes. Calculation of the right-side flux is associated with the speed $\mathbf{u} - |\mathbf{u}|$. On the other hand, left-side flux is associated with the speed $\mathbf{u} + |\mathbf{u}|$. Finally, the source term in the equation of level set method is calculated through the following equation:

$$\hat{F}_{i+1/2} = \frac{1}{2}\left(\hat{F}^R_{i+1/2} + \hat{F}^L_{i+1/2}\right) \tag{41}$$

3.1.1.3. Boundary condition for DRP-CRWENO4 scheme   This scheme is a tridiagonal system of equations and can be represented as

$$\begin{bmatrix} 1 & 0 & 0 & \dots & \dots & \dots & 0 \\ a & b & c & 0 & \dots & \dots & 0 \\ \cdot & & \cdot & & & & \cdot \\ \cdot & & & \cdot & & & \cdot \\ \cdot & & & & \cdot & & \cdot \\ 0 & \dots & \dots & 0 & a & b & c \\ 0 & \dots & \dots & \dots & 0 & 0 & 1 \end{bmatrix} \begin{bmatrix} \hat{F}_{1/2} \\ \cdot \\ \cdot \\ \hat{F}_{i+1/2} \\ \cdot \\ \cdot \\ \hat{F}_{N+1/2} \end{bmatrix} = \begin{bmatrix} \bar{r}^{WENO5}_{1/2} \\ \cdot \\ \cdot \\ \bar{r}^{DRP-CRWENO4}_{i+1/2} \\ \cdot \\ \cdot \\ \bar{r}^{WENO5}_{N+1/2} \end{bmatrix}, \tag{42}$$

where a, b, c are the coefficients, as shown in Eq. (33) and Eq. (38). It should be noted that numerical fluxes at the boundary interfaces are reconstructed using the WENO5 procedure. That is,

$$\hat{F}^L_{i+\frac{1}{2}} = \frac{\omega_1}{3}F_{i-2} - \frac{1}{6}\left(7\omega_1 + \omega_2\right)F_{i-1} + \frac{1}{6}\left(11\omega_1 + 5\omega_2 + 2\omega_3\right)F_i$$

$$+ \frac{1}{6}\left(2\omega_2 + 5\omega_3\right)F_{i+1} - \frac{\omega_3}{6}F_{i+2},$$

$$\hat{F}^R_{i+\frac{1}{2}} = -\frac{\widetilde{\omega}_3}{6}F_{i-1} + \frac{1}{6}\left(2\widetilde{\omega}_2 + 5\widetilde{\omega}_3\right)F_i + \frac{1}{6}\left(11\widetilde{\omega}_1 + 5\widetilde{\omega}_2 + 2\widetilde{\omega}_3\right)F_{i+1} \tag{43}$$

$$- \frac{1}{6}\left(7\widetilde{\omega}_1 + \widetilde{\omega}_2\right)F_{i+2} + \frac{\widetilde{\omega}_1}{3}F_{i+3},$$

where ω and $\widetilde{\omega}$ are defined in Eq. (34) and Eq. (39), respectively. Here, $\bar{r}$ is the right-hand side of the reconstruction flux in the framework of the DRP-CRWENO4 or WENO5 scheme, as shown in Eq. (33), (38), or (43). In the above WENO5 scheme

framework, the required values for the WENO5 scheme at the boundaries are provided using ghost points. The tridiagonal matrix algorithm (TDMA) method, which is a simplified form of Gaussian elimination, is used to solve the tridiagonal coefficient matrix.

3.1.2. Approximation of spatial derivatives for the re-initialization equation

Equation (6) for the two-dimensional case can be expressed in a semi-discrete form:

$$\frac{d\phi}{dt} + H_G\left(\phi_x^+, \phi_x^-, \phi_y^+, \phi_y^-\right) = 0, \tag{44}$$

where H_G is the Godunov Hamiltonian. The spatial discretizations $\phi_{x,i}^-$ (left-biased stencil from $i-3$ to $i+2$) and $\phi_{x,i}^+$ (right-biased stencil from $i-2$ to $i+3$) in Eq. (6) are approximated using the fifth-order WENO5 scheme [49]

$$\phi_{x,i}^- = \frac{1}{12}\left(-\frac{\triangle^+\phi_{i-2}}{\triangle x} + 7\frac{\triangle^+\phi_{i-1}}{\triangle x} + 7\frac{\triangle^+\phi_i}{\triangle x} - \frac{\triangle^+\phi_{i+1}}{\triangle x}\right)$$
$$-\phi^{WENO}\left(\frac{\triangle^-\triangle^+\phi_{i-2}}{\triangle x}, \frac{\triangle^-\triangle^+\phi_{i-1}}{\triangle x}, \frac{\triangle^-\triangle^+\phi_i}{\triangle x}, \frac{\triangle^-\triangle^+\phi_{i+1}}{\triangle x}\right) \tag{45}$$

and

$$\phi_{x,i}^+ = \frac{1}{12}\left(-\frac{\triangle^+\phi_{i-2}}{\triangle x} + 7\frac{\triangle^+\phi_{i-1}}{\triangle x} + 7\frac{\triangle^+\phi_i}{\triangle x} - \frac{\triangle^+\phi_{i+1}}{\triangle x}\right)$$
$$-\phi^{WENO}\left(\frac{\triangle^-\triangle^+\phi_{i+2}}{\triangle x}, \frac{\triangle^-\triangle^+\phi_{i+1}}{\triangle x}, \frac{\triangle^-\triangle^+\phi_i}{\triangle x}, \frac{\triangle^-\triangle^+\phi_{i-1}}{\triangle x}\right) \tag{46}$$

where $\triangle^+\phi_k = \phi_{k+1} - \phi_k$, $\triangle^-\phi_k = \phi_k - \phi_{k-1}(k = i-3 \sim i+2)$. Note that ϕ^{WENO} is a nonlinear function and is expressed as follows in terms of $\mathbf{a}, \mathbf{b}, \mathbf{c}, \mathbf{d}$:

$$\phi^{WENO}(\mathbf{a}, \mathbf{b}, \mathbf{c}, \mathbf{d}) = \frac{1}{3}\bar{\omega}_0(\mathbf{a} - 2\mathbf{b} + \mathbf{c}) + \frac{1}{6}\left(\bar{\omega}_2 - \frac{1}{2}\right)(\mathbf{b} - 2\mathbf{c} + \mathbf{d}). \tag{47}$$

The weighting factors $\bar{\omega}_0$ and $\bar{\omega}_2$ are defined as

$$\bar{\omega}_0 = \frac{\alpha_0}{\alpha_0 + \alpha_1 + \alpha_2}, \bar{\omega}_2 = \frac{\alpha_2}{\alpha_0 + \alpha_1 + \alpha_2} \tag{48}$$

with

$$\alpha_0 = \frac{1}{(\varepsilon + IS_0)^2}, \alpha_1 = \frac{6}{(\varepsilon + IS_1)^2}, \alpha_2 = \frac{3}{(\varepsilon + IS_2)^2}, \tag{49}$$

where ε is chosen to prevent division by zero, according to the suggestion of Jiang and Shu [44]. The smoothness indicators are defined as follows:

$$IS_0 = 13(\mathbf{a} - \mathbf{b})^2 + 3(\mathbf{a} - 3\mathbf{b})^2,$$
$$IS_1 = 13(\mathbf{b} - \mathbf{c})^2 + 3(\mathbf{b} + \mathbf{c})^2, \tag{50}$$
$$IS_2 = 13(\mathbf{c} - \mathbf{d})^2 + 3(3\mathbf{c} - \mathbf{d})^2.$$

Note that $|\nabla\phi|$ in Eq. (6) can be defined as [50]

$$|\nabla\phi| = \begin{cases} \bar{S}(\phi_0)\left(\sqrt{[\max(\bar{a}^-, \bar{b}^+)]^2 + [\max(\bar{c}^-, \bar{d}^+)]^2}\right); & \text{if } \phi_0 \geq 0, \\ \bar{S}(\phi_0)\left(\sqrt{[\max(\bar{a}^+, \bar{b}^-)]^2 + [\max(\bar{c}^+, \bar{d}^-)]^2}\right); & \text{otherwise,} \end{cases} \tag{51}$$

where $(\bar{a})^+ = \max(a, 0)$ and $(\bar{a})^- = -\min(a, 0)$. The detailed numerical integration over the domain Ω in Eq. (7) is computed using a 27-point stencil in three dimensions:

$$\int_{\Omega_{ijk}} \bar{g} \approx 51\bar{g}_{ijk} + \sum_{m,n,l=-1;(m,n,l)\neq(0,0,0)}^{1} \bar{g}_{i+m, j+n, k+l}. \tag{52}$$

3.1.3. Time marching scheme

An explicit third-order total variation diminishing Runge–Kutta (TVD-RK3) time discretization [50] is used for solving Eq. (6) and Eq. (12). For example, both equations can be written as the following ODEs:

$$\frac{d\phi}{dt} = L(\phi). \tag{53}$$

The TVD-RK3 scheme is then applied over the following three solution steps

$$\phi^{(1)} = \phi^{(n)} + \Delta t L(\phi^{(0)}), \tag{54}$$

$$\phi^{(2)} = \frac{3}{4}\phi^{(n)} + \frac{1}{4}\phi^{(1)} + \frac{1}{4}\Delta t L(\phi^{(1)}), \tag{55}$$

$$\phi^{(n+1)} = \frac{1}{3}\phi^{(n)} + \frac{2}{3}\phi^{(2)} + \frac{2}{3}\Delta t L(\phi^{(2)}). \tag{56}$$

3.2. Navier–Stokes equation solver

3.2.1. Projection method

The discretization procedure used to approximate Eq. (10) is based on the projection method. Given $\mathbf{u}^n$ and $\mathbf{f}^n$, the second-order Adams–Bashforth scheme for time advancement can be written as follows:

$$\frac{\mathbf{u}^{n+1} - \mathbf{u}^n}{\Delta t} + \mathbf{f}^n + \frac{1}{\rho(\phi)}\frac{\delta\mathbf{x}}{\Delta\mathbf{x}}P^{n+\frac{1}{2}} = 0, \tag{57}$$

where $\delta\mathbf{x}$ is the first-order central-difference operator and

$$\mathbf{f}^n = \frac{3}{2}\mathbf{A}^n - \frac{1}{2}\mathbf{A}^{n-1}, \tag{58}$$

where $\mathbf{f}(\equiv (f, g, h))$ are vectors in the x, y, and z direction. In Eq. (58), $\mathbf{A}$ denotes terms treated by the Adams–Bashforth scheme

$$\mathbf{A} = \mathbf{u} \cdot \nabla\mathbf{u} - \frac{1}{\rho(\phi)}\nabla \cdot [\mu(\phi)(\nabla\mathbf{u} + (\nabla\mathbf{u})^T)] - \mathbf{g}. \tag{59}$$

It should be noted that the pressure source terms in the above equation are ignored. The values for the next time step $\mathbf{u}^{n+1}$ can be obtained when the pressure Poisson equation is solved to enforce the continuity equation.

3.2.2. Momentum equation solver

For the convection terms in Eq. (10), it is essential that the upwind principle be retained to enable the suppression of convective oscillations. For example, the convection terms $u\frac{\partial u}{\partial x}$ in the x-direction momentum equation can be approximated by a second-order upwinding scheme

$$u\frac{\partial u}{\partial x} = \frac{1}{2}(u^+(3u_{i,j,k} - 4u_{i-1,j,k} + u_{i-2,j,k}) + u^-(-u_{i+2,j,k} + 4u_{i+1,j,k} - 3u_{i,j,k})), \tag{60}$$

where $u^+ = \frac{1}{2}\left(u_{i,j,k} + |u_{i,j,k}|\right)$ and $u^- = \frac{1}{2}\left(u_{i,j,k} - |u_{i,j,k}|\right)$. The diffusion terms in Eq. (10) are discretized with the second-order central-difference scheme.

3.2.3. Poisson equation solver

For solving the pressure field, a projection method is performed to solve the time-dependent incompressible two-phase flow solutions. By considering the divergence operator in Eq. (57) and forcing the continuity equation to zero as the constraint condition, we get:

$$\nabla \cdot \mathbf{u}^{n+1} = 0. \tag{61}$$

The Poisson equation for $p^{n+\frac{1}{2}}$ can be derived as

$$\left(\frac{\delta x}{\Delta x}\frac{1}{\rho(\phi)}\frac{\delta x}{\Delta x} + \frac{\delta y}{\Delta y}\frac{1}{\rho(\phi)}\frac{\delta y}{\Delta y} + \frac{\delta z}{\Delta z}\frac{1}{\rho(\phi)}\frac{\delta z}{\Delta z}\right)p^{n+1/2} = \mathbf{RHS}, \tag{62}$$

where $\mathbf{RHS} = \frac{\delta x}{\Delta x}\left(\frac{u^n}{\Delta t} - f^n\right) + \frac{\delta y}{\Delta y}\left(\frac{v^n}{\Delta t} - g^n\right) + \frac{\delta z}{\Delta z}\left(\frac{w^n}{\Delta t} - h^n\right)$. Note that $p^{n+\frac{1}{2}}$ must satisfy the Neumann boundary conditions at all walls shown below:

$$\frac{\partial p^{n+\frac{1}{2}}}{\partial \mathbf{x}} = -\left(\frac{\mathbf{u}^{n+1} - \mathbf{u}^n}{\triangle t}\right) + \mathbf{f}^n \quad \text{at } \mathbf{x} = 0, L_{\mathbf{x}}. \tag{63}$$

The Poisson equation (i.e., Eq. (62)) can be expressed as its equivalent discretized equation by using a second-order central-difference formulation

$$a P_{i-1,j,k} + b P_{i+1,j,k} + c P_{i,j,k} + d P_{i,j-1,k} + e P_{i,j+1,k} + f P_{i,j,k-1} + g P_{i,j,k+1} = (\mathbf{RHS})_{i,j,k}, \tag{64}$$

where $a = b = \frac{1}{\rho \triangle x^2}$, $d = e = \frac{1}{\rho \triangle y^2}$, $f = g = \frac{1}{\rho \triangle z^2}$, and $c = -(a+b+d+e+f+g) = -(\frac{1}{\rho \triangle x^2} + \frac{1}{\rho \triangle y^2} + \frac{1}{\rho \triangle z^2})$. The point successive over-relaxation method is used to optimally solve the tridiagonal and sparse matrix for Eq. (64)

$$P_{i,j,k}^{m+1} = \omega P_{i,j,k}^{m+1} + (1 - \omega) P_{i,j,k}^m, \tag{65}$$

where $\omega = 1.5$ is the coefficient of relaxation and m is the iteration counter. The solutions calculated from two consecutive iterations $p^{m+1} - p^m$ fall below the user's specified tolerance

$$|P_{i,j,k}^{m+1} - P_{i,j,k}^m| \leq 10^{-4}. \tag{66}$$

3.2.4. Numerical stability conditions

Because the developed Adams–Bashforth solution procedure is explicit, the computational time step should be limited by numerical stability conditions for flow computation. The restrictions for the advection, diffusion, and gravity terms are

$$\triangle t_u = \min_{\Omega}\left(|\frac{u}{\triangle x}|, |\frac{v}{\triangle y}|, |\frac{w}{\triangle z}|\right), \tag{67}$$

$$\triangle t_\mu = \min_{\Omega_\delta} \frac{Re}{2\left[\frac{1}{\triangle x^2} + \frac{1}{\triangle y^2} + \frac{1}{\triangle z^2}\right]}, \tag{68}$$

$$\triangle t_g = \min_{\Omega}\sqrt{\frac{\triangle z}{g}}. \tag{69}$$

Finally, the time step restriction should satisfy the following condition:

$$\triangle t^{n+1} = \min(\triangle t_u, \triangle t_\mu, \triangle t_g). \tag{70}$$

3.3. Solution procedure

For the sake of clarity, the proposed level set method solver and Navier–Stokes equation algorithm for a one time step loop are summarized as follows:

(1) Solve the level set equation (i.e., Eq. (12)) using DRP-CRWENO4 and TVD-RK3 schemes to obtain the level set solution $\widetilde{\phi}^{n+1}$.
(2) Solve the re-initialization equation (i.e., Eq. (6)) using the WENO5 and TVD-RK3 schemes to retain $\widetilde{\phi}^{n+1}$ as the distance function ϕ^{n+1}.
(3) Define the density $\rho(\phi)$ and viscosity $\mu(\phi)$ in Eq. (11).
(4) Compute the convection and diffusion terms in the momentum equation.
(5) Solve the pressure Poisson equation (i.e. Eq. (62)) using the point successive over-relaxation method to obtain $p^{n+\frac{1}{2}}$.
(6) Update the velocity field using Eq. (57).

4. Validation studies

The behavior of the DRP-CRWENO4 scheme is shown by a number of benchmark advection tests. The computational efficiencies of the DRP-CRWENO4 and WENO5 schemes are tested for a one-dimensional advection problem using a Core i7, 4.0 GHz computer with 64.0 GB of RAM. To measure the mass conservation property, we define the mass error as

$$\mathbf{M}_{error} = \int_{\Omega} \bar{H}(\phi)\, d\Omega - 1. \tag{71}$$

Table 1
Rates of convergence and CPU times of DRP-CRWENO4 and WENO5 schemes for one-dimensional advection problem #1. Note that CPU time of 6400 grid is measured in the program using quadruple-precision, the others are only double-precision.

Scheme	Grids	L_2 norms	R.O.C.	CPU time (s)
WENO5	200	1.6094×10^{-8}		0.20
	400	4.9955×10^{-10}	5.00	0.76
	600	6.5742×10^{-11}	5.00	1.70
	800	1.5619×10^{-11}	4.99	3.01
	1000	5.1301×10^{-12}	4.99	4.73
	1200	2.0651×10^{-12}	4.99	6.76
	1400	9.6603×10^{-13}	4.93	9.23
	1600	5.0024×10^{-13}	4.93	12.34
	6400	4.8272×10^{-16}	5.01	40068.7
DRP-CRWENO4	200	1.0921×10^{-9}		0.56
	400	6.7243×10^{-11}	4.02	1.90
	600	1.3254×10^{-11}	4.01	4.06
	800	4.1995×10^{-12}	3.99	7.28
	1000	1.7428×10^{-12}	3.94	11.14
	1200	8.3550×10^{-13}	4.03	16.37
	1400	4.4061×10^{-13}	4.15	21.92
	1600	2.5240×10^{-13}	4.17	28.90
	6400	1.0378×10^{-15}	3.96	47499.9

4.1. One-dimensional advection problem #1

A one-dimensional advection equation $u_t + cu_x = 0$ with $c = 1$ is solved on the interval $[-1, 1]$, and the L2-error $\sum \sqrt{(\phi - \phi_{exact})^2}$ is computed at $t = 2.0$ subject to the following smooth initial condition:

$$u(x, 0) = \sin(\pi x - \frac{\sin(\pi x)}{\pi}). \tag{72}$$

We check the convergence rate for this scalar test problem with Courant–Friedrichs–Lewy (CFL) number 0.1. The corresponding spatial rates of convergence for the DRP-CRWENO4 and WENO5 schemes are given in Table 1. As the computational grid is refined, we see that the DRP-CRWENO4 scheme converges to a fourth-order problem.

4.2. One-dimensional advection problem #2

A one-dimensional equation $\phi_t + c\phi_x = 0$ is also considered with the following initial condition [44]

$$\phi(x) = \begin{cases} \exp(-\log(2)\frac{(x+7)^2}{0.0009}); & -0.8 \leq x \leq -0.6, \\ 1; & -0.4 \leq x \leq -0.2, \\ 1 - |10(x - 0.1)|; & 0 \leq x \leq 0.2, \\ \frac{1 - 100(x - 0.5)^2}{2}; & 0.4 \leq x \leq 0.6, \\ 0; & \text{otherwise.} \end{cases} \tag{73}$$

This initial condition consists of various shapes, including a discontinuous square pulse, and different continuous but narrow profiles. A periodic boundary condition is imposed in this study. The time step is chosen to be $\Delta t = 0.1\Delta x$.

We show the numerical results at $t = 2.0$ in Fig. 1 and Fig. 2, with the domain $[-1, 1]$ being divided into uniform grids 50 and 100, respectively. Comparing the magnitude of errors produced by the WENO5 and DRP-CRWENO4 schemes for the other continuous wave shows that the DRP-CRWENO4 scheme performs better. The computational costs of using the DRP-CRWENO4 and WENO5 schemes are compared based on different grids, as shown in Table 2.

4.3. Two-dimensional vortex deforming problem

A two-dimensional test problem for reversible vortex flow in a square domain $[1 \times 1]$ is considered. The center of this velocity field, defined for a circle of radius 0.15, is initially $(0.5, 0.75)$. This vortex problem [12,13,27,51] under a divergence-free velocity field is given by

$$u(x, y, t) = \sin(\pi x)^2 \sin(2\pi y) \cos(\frac{\pi t}{T}),$$
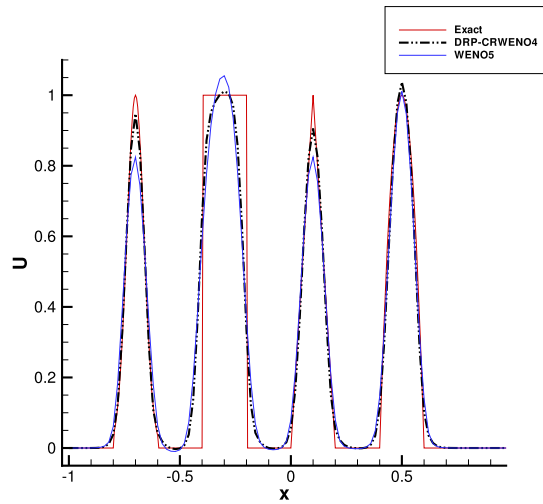$$v(x, y, t) = -\sin(\pi y)^2 \sin(2\pi x) \cos(\frac{\pi t}{T}). \tag{74}$$

Fig. 1. Predicted results for one-dimensional advection problem #2 at $t = 2.0$ with the 50 grids solution.
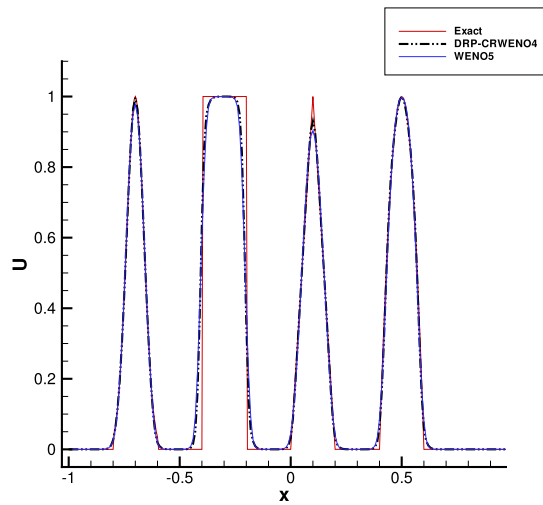

Fig. 2. Predicted results for one-dimensional advection problem #2 at $t = 2.0$ with the 100 grids solution.

Table 2
Computational costs for DRP-CRWENO4 and WENO5 schemes for one-dimensional advection problem #2.

Scheme	Grids	CPU times (s)
WENO5	200	1.4062×10^{-1}
	400	5.1562×10^{-1}
	800	2.0938×10^{0}
	1600	8.4531×10^{0}
DRP-CRWENO4	200	2.3438×10^{-1}
	400	8.5938×10^{-1}
	800	3.4219×10^{0}
	1600	1.4250×10^{1}
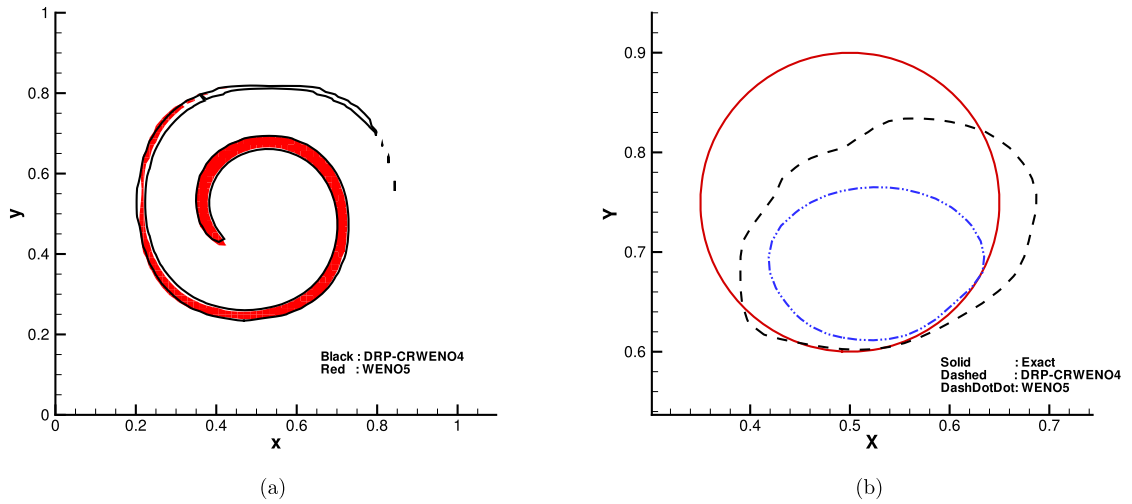
Fig. 3. Coarse grid solution of vortex deforming problem. (a) $t = \frac{T}{2} = 4.0$; (b) $t = T = 8.0$.
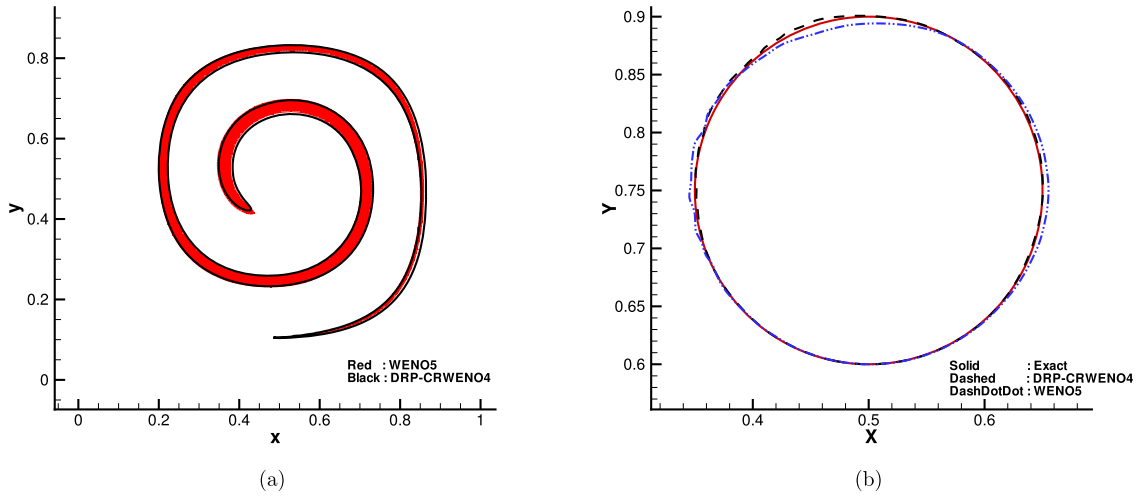
Fig. 4. Fine grid solution of vortex deforming problem. (a) $t = T/2 = 4.0$; (b) $t = T = 8.0$.

Table 3
Error estimation in the test of one period of 2D vortex deforming problem.

Scheme	Grids	Area loss (%)	L_1 error	Order	CPU time (s)
WENO5	64^2	63.436	4.370×10^{-2}	N/A	1.026
	128^2	5.6905	1.221×10^{-2}	1.84	5.691
	256^2	-0.699	2.228×10^{-3}	2.45	40.32
	512^2	0.082	3.700×10^{-4}	2.59	785.1
	1024^2	0.029	1.001×10^{-4}	1.88	7162
DRP-CRWENO4	64^2	26.087	3.174×10^{-2}	N/A	1.672
	128^2	-0.934	7.690×10^{-3}	2.04	10.23
	256^2	-0.647	6.686×10^{-4}	3.52	72.68
	512^2	-0.009	1.144×10^{-4}	2.54	1024
	1024^2	0.004	5.722×10^{-5}	0.99	9578
HPLS	64^2	1.81	0.003	N/A	–
	128^2	0.71	0.001	1.1	–
	256^2	0.35	5.09×10^{-4}	1.4	–

(a) Coarse Grid

(b) Fine Grid
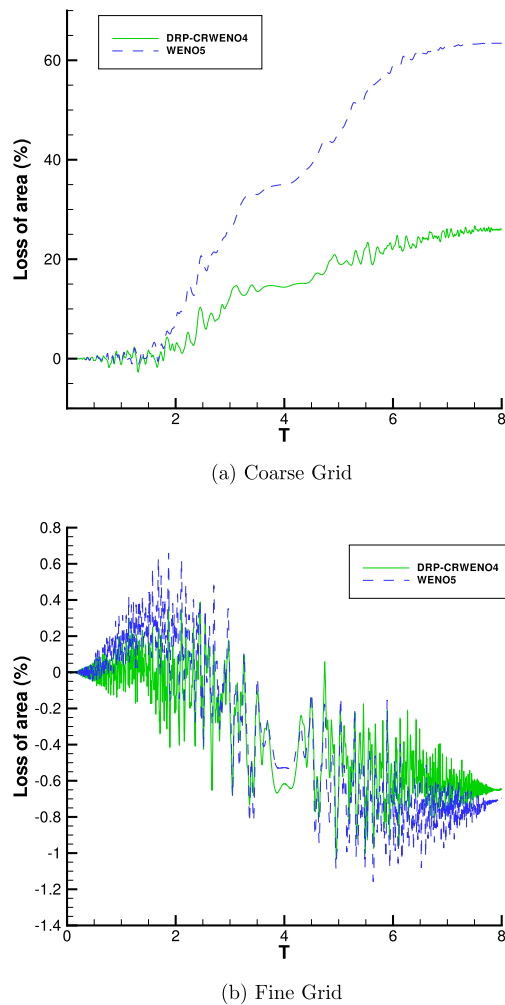
Fig. 5. Mass loss of vortex deforming problem.

It should be noted that T is the period of reversed vortex flow and is set at 8. In other words, the flow field was reversed so that the exact solution at $t = 8$ would theoretically coincide with the initial condition.

The results predicted using the DRP-CRWENO4 and WENO5 schemes for 64×64 and 256×256 grids with $\Delta t = 0.01\Delta x$ are plotted in Fig. 3 and Fig. 4 for solutions at $t = \frac{T}{2} = 4.0$ and $t = T = 8.0$, respectively. DRP-CRWENO4 shows better conservation of mass in comparison with WENO5 for both fine and coarse grids, as shown in Fig. 5. In Table 3, the DRP-CRWENO4 scheme loses approximately 0.004% of mass in the 1024×1024 grids solution, which is much better than the 0.029% mass loss for WENO5. From Fig. 4, we see that higher resolution results in sharper tail shapes at $t = 4.0$ and perfect circular shapes at $t = 8.0$. This section demonstrates that DRP-CRWENO4 has better conservation of mass and the ability to accurately capture vortex deformation in comparison with WENO5.

The mass loss and L_1 error results for three grids 64^2, 128^2, 256^2, 512^2, 1024^2 are tabulated in Table 3. The predicted L_1 error is defined by

$$\frac{1}{L} \int_{\Omega} |\bar{H}(\phi_{Numerical}) - \bar{H}(\phi_{Exact})| d\Omega, \tag{75}$$

where L is the perimeter. Calculation results show that the mass loss is significantly increased using the WENO scheme due to its numerical dissipation. Table 3 also shows that the HPLS method [37] can be satisfactorily applied to the level set advection equation for mass conservation.
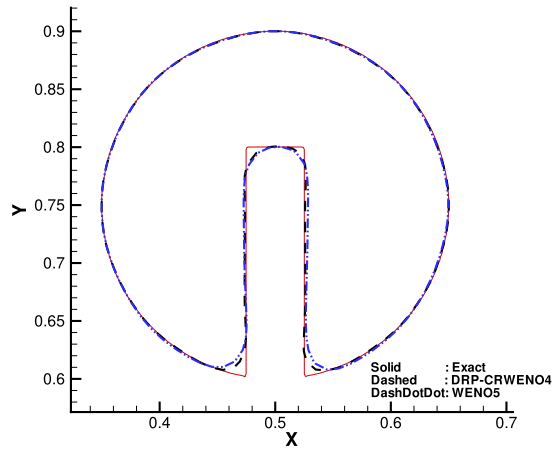
(a) Grid: 100×100
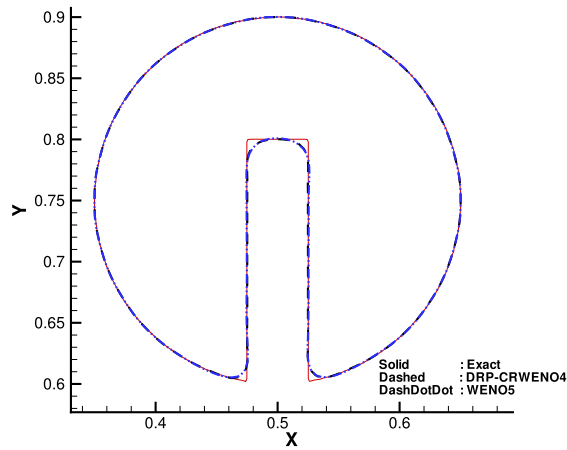
(b) Grid: 200×200

Fig. 6. Solution after one rotation in fine and coarse grids. (a) Coarse grid; (b) Fine grid.

4.4. Zalesak's disk problem

The Zalesak's disk problem is considered to verify the proposed DRP-CRWENO4 advection scheme for the computational domain 1×1 [12,13,27,51]. The disk has a radius of 0.15, a slot length of 0.25, and a width of 0.05. It is made to rotate about the point $(0.50, 0.75)$ with the constant velocity field given by $u = -\frac{2\pi(y-0.5)}{5}$ and $v = \frac{2\pi(x-0.5)}{5}$. We perform calculations on two different grids (100×100 and 200×200) with $\Delta t = 0.01\Delta x$.

Solutions after one revolution are compared with the initial shape to show the ability of the DRP-CRWENO4 and WENO5 schemes in solving the advection problem. Fig. 6 shows a comparison of results obtained in fine and coarse grids; the DRP-CRWENO4 scheme shows better agreement with the exact solution schematic for coarse grid. From Fig. 7, mass conservation performance is better for DRP-CRWENO4 than WENO5. Table 4 shows the L_1 error norms computed at a time after one or two rotations. It is revealed that L_1 error for the WENO5 scheme is larger than that for the DRP-CRWENO4 scheme on all grids, and that the DRP-CRWENO4 scheme is in reasonable agreement with the exact solution.

In Table 4 for the 2D Zalesak's disk test, one can find slight area gain by DRP-CRWENO4 compared to WENO5 and HPLS. The proposed DRP-CRWENO4 scheme has less dissipation, and hence oscillations may exist in the solution without any artificial viscosity being added in this two-dimensional case. This could be one of the reasons why mass is slightly gained in the proposed scheme for this case. Another reason may be that the mass change given in Table 4 is an overall result, reflecting the sum of all local mass gain and local mass loss. In Fig. 6(a) for specific, the slot in the disk gains mass at its closed end (close to the disk center), and loses mass at its open end (at the disk border), and the sum of the two local changes is manifested as an overall gain on the whole.
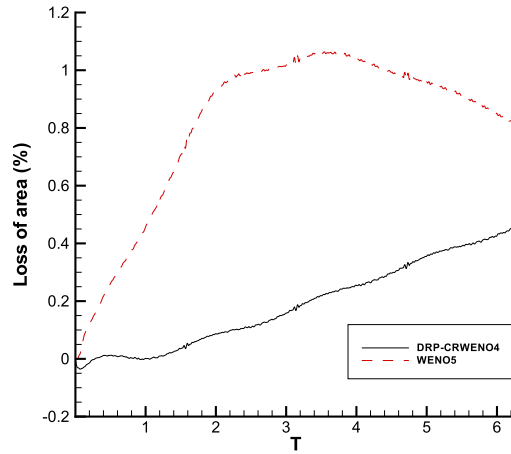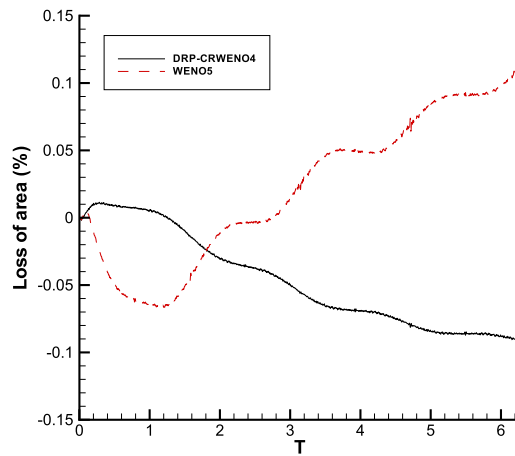
(a) Grid: 100×100

(b) Grid: 200×200

Fig. 7. Mass loss in fine and coarse grid during the rotation. (a) Coarse grid; (b) Fine grid.

4.5. Three-dimensional vortex deforming problem

A three-dimensional single vortex deforming problem was considered by [13,37] to evaluate capability of the proposed level set method (LS) and the hybrid particle level set (HPLS) method [37] under cases of strong interface deformation. A sphere with radius 0.15 is initially placed at center point $(0.35, 0.35, 0.35)$ in a unit cube. Velocity components for this problem are given by

$$u(x, y, z, t) = 2\sin(\pi x)^2 \sin(2\pi y) sin(2\pi z) \cos(\frac{\pi t}{T}),$$
$$v(x, y, z, t) = -\sin(2\pi x) \sin(\pi y)^2 sin(2\pi z) \cos(\frac{\pi t}{T}),$$
$$w(x, y, z, t) = -\sin(2\pi x) \sin(2\pi y) sin(\pi z)^2 \cos(\frac{\pi t}{T}),$$

(76)

where t is the time at any instant. Note that T is the time after which the sphere reverses back to its initial position, which is set to be 3.0. Simulation results using the proposed LS method in $100 \times 100 \times 100$ mesh points are compared with the solution using HPLS method of Enright et al. [37], which are shown in Fig. 8(a) and 8(b) respectively. The snapshots of the interface obtained from the proposed LS method matches not so well with the numerical results of [37]. For HPLS method, however, the negative domain gets expanded to the extent where the grid spacing at $t = \frac{T}{2}$ exceeds its minimum thickness. The expansion is then followed by mass loss, which primarily comes as a result of the period when particles are most likely to be misplaced during a particle reseeding procedure. Simulation using the proposed DRP-CRWENO4 and previous WENO5

Table 4
Error estimation in the test of 2D Zalesak's disk.

Scheme	Grids	Area loss (%)	L_1 error	Order	CPU time (s)
One revolution					
WENO5	50	−5.949	8.800×10^{-3}	N/A	0.450
	100	0.801	2.400×10^{-3}	1.84	2.179
	200	0.118	5.000×10^{-5}	2.45	13.89
	400	−0.0025	6.250×10^{-6}	2.59	211.4
	800	0.00049	7.813×10^{-6}	1.88	2539
DRP-CRWENO4	50	−0.015	1.700×10^{-3}	N/A	0.723
	100	0.448	8.000×10^{-4}	2.04	3.960
	200	−0.0935	5.000×10^{-5}	3.52	26.72
	400	−0.0012	6.250×10^{-6}	2.54	310.7
	800	0.00026	1.563×10^{-6}	0.99	3452
HPLS [37]	50	14.9	0.59	N/A	–
	100	0.31	0.07	3.1	–
	200	0.20	0.02	1.5	–
Two revolutions					
WENO5	50	−8.462	1.120×10^{-2}	N/A	0.891
	100	2.047	2.600×10^{-3}	2.10	4.402
	200	0.332	1.000×10^{-4}	4.70	27.81
	400	−0.0538	1.875×10^{-5}	2.41	413.1
	800	−0.00358	9.375×10^{-6}	1.00	5076
DRP-CRWENO4	50	−0.784	2.000×10^{-3}	N/A	1.389
	100	0.842	1.800×10^{-3}	0.15	7.851
	200	−0.0968	5.000×10^{-5}	5.16	53.53
	400	0.01003	7.250×10^{-6}	2.78	607.3
	800	0.0004	2.163×10^{-6}	1.75	6877
HPLS [37]	50	16.2	0.62	N/A	–
	100	0.72	0.09	2.8	–
	200	0.38	0.03	1.4	–

schemes in $100 \times 100 \times 100$ mesh points are also carried out. Mass loss at $t = T = 3.0$ reaches 28.68% for the WENO5 scheme and only 10.86% for the DRP-CRWENO4 scheme. The HPLS method has the best mass preservation with only 2% loss. It is shown that the mass loss is greatly reduced for both DRP-CRWENO4 and HPLS method. The solution using the WENO5 scheme loses significant amount of mass owing to its numerical dispersion and dissipation error. More accurately, the DRP-CRWENO5 scheme solution is quite accurate for approximation of advection terms in the level set equation.

4.6. Three-dimensional Zalesak's Sphere problem

The Zalesak's sphere which has been successfully used in verifying the developed advection DRP-CRWENO4 scheme is a well-known benchmark problem in the three-dimensional case. The sphere, which has a slot 5 grid cells wide and 12.5 grid cells deep, is initially located at $(0.5, 0.75, 0.5)$ on a square of 100 grid cell domain. The sphere rotates in the $z = 0.5$ plane at point $(0.5, 0.5, 0.5)$ and the prescribed velocity field is given by

$$u(x, y, z, t) = \frac{\pi}{314}(0.5 - y),$$

$$v(x, y, z, t) = \frac{\pi}{314}(x - 0.5),$$

$$w(x, y, z, t) = 0.$$

(77)

It is noted that the sphere makes one rotation per 628 time units. Fig. 9 shows predicted results using DRP-CRWENO4 scheme as compared with the results using the proposed LS and HPLS methods in $100 \times 100 \times 100$ mesh points. Good agreement can be found between HPLS and present predicted solutions. However, the proposed LS method shows more damping in convex and concave regions of the slot than the HPLS method owing to the inward and outward dissipation errors respectively. The mass error of the proposed LS method is approximately 0.03% less than that of the HPLS method, which produces relatively smaller error for $100 \times 100 \times 100$ grids. It is noted that flotsam and jetsam phenomena occur in convex and concave regions of slot respectively [37] although the proposed LS method shows excellent mass conservation property.
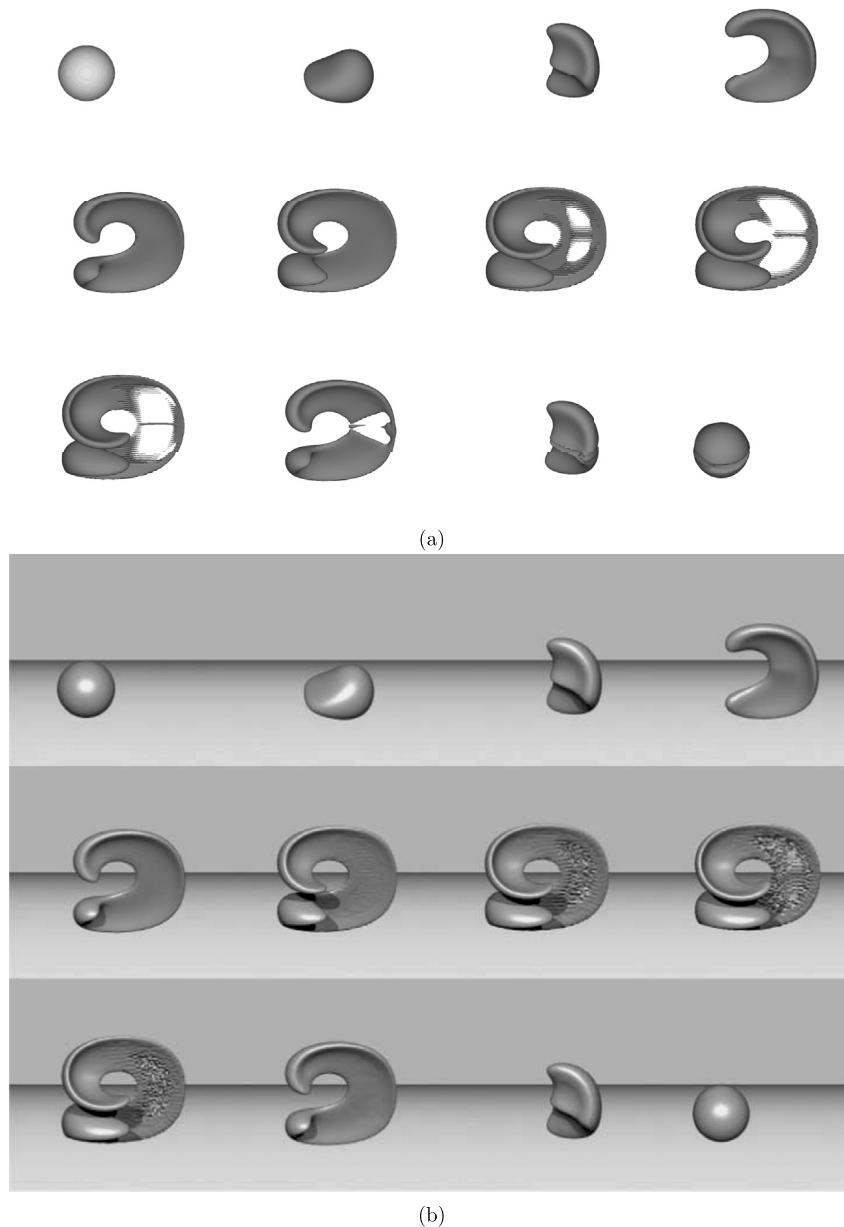
(a)

(b)

Fig. 8. Evolution of 3D deformation at the time $t = 0.0, 0.2, 0.4, 0.6, 0.8, 1.0, 1.2, 1.4, 1.8, 2.2, 2.6, 3.0$, corresponding to each subfigure from left to right, top to bottom. (a) Present results; (b) Solutions by using HPLS method [37].

5. Numerical results

With the successful verification of the advection scheme, four dam-break problems with large density variations across the interface are investigated. This is done to justify the interface-preserving level set method and incompressible flow solvers. In the following literature, the unit grid is defined as the number of cells per unit length and has identical value with $\frac{1}{\mathbf{h}}$, where $\mathbf{h} = dx = dy = dz$ is the mesh size. The computational domain, number of uniform grids values and time-step size Δt are shown in Table 5 for all dam-break problems. In addition, all the simulations are carried out with density ratio $\frac{\rho_G}{\rho_L} = 0.001$ and viscosity ratio $\frac{\mu_G}{\mu_L} = 0.01$. The atmospheric pressure is $1.013 \times 10^5 \, Pa$ in our program, which is non-dimensionlized using the characteristic value $\rho_L U^2$, where U is the characteristic velocity.

(a)

(b)
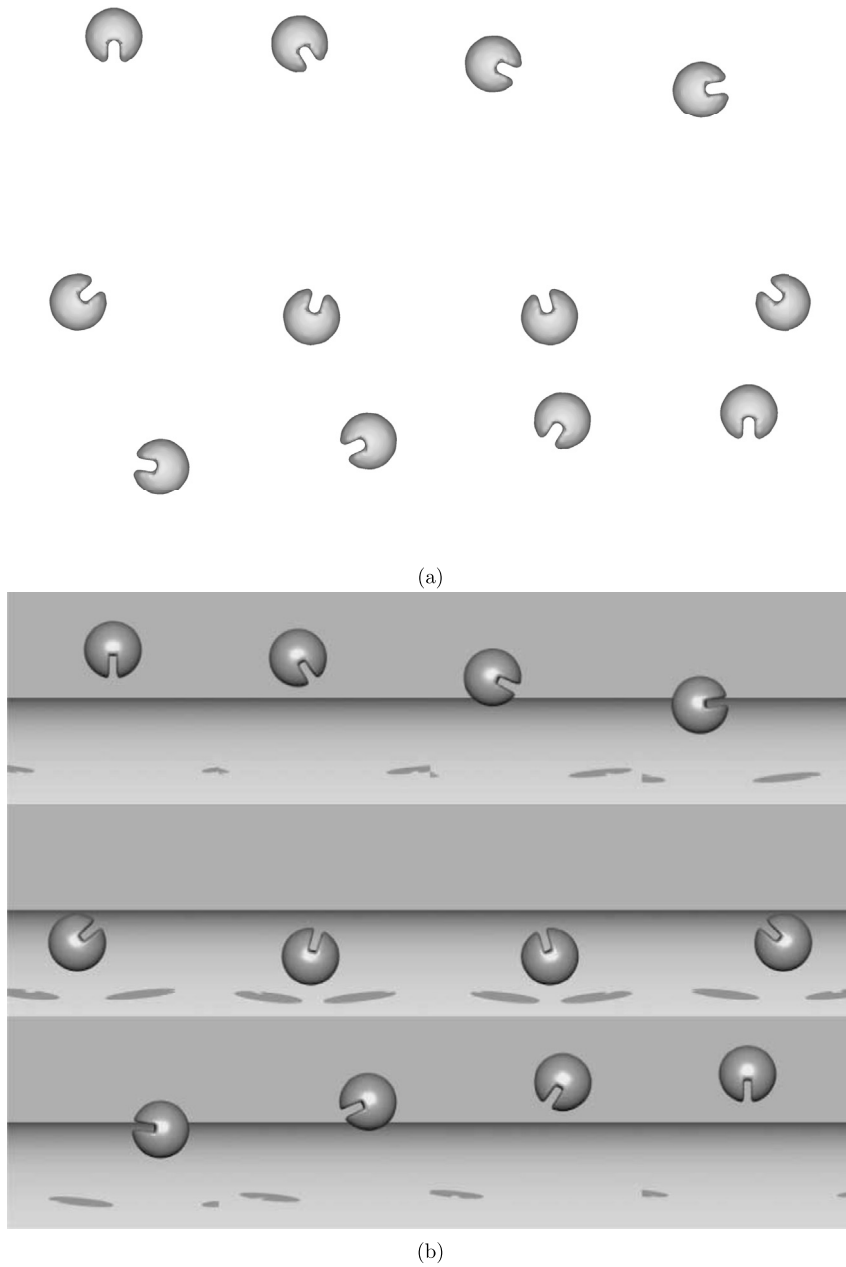
Fig. 9. Evolution of Zalesak's sphere after one rotation ($t = 200\pi$). Note that the time interval is $\frac{50\pi}{3}$ corresponding to each subfigure from left to right, top to bottom. (a) Present results; (b) Solutions by using HPLS method [37].

Table 5
The four simulations performed in highest resolution and time-step sizes.

Section	Computational domain	Grids	Time-step size Δt
5.1	$5 \times 1.25 \times 1$	$250 \times 63 \times 50$	$\Delta t = 0.01\Delta x$
5.2	$10 \times 1 \times 1.2$	$500 \times 50 \times 60$	$\Delta t = 0.01\Delta x$
5.3	$3 \times 2 \times 1$	$150 \times 100 \times 50$	$\Delta t = 0.01\Delta x$
5.4	$3.25 \times 1 \times 1$	$162 \times 50 \times 50$	$\Delta t = 0.01\Delta x$

(a) t=0.0

(b) t=1.8

(c) t=3.6

(d) t=5.4

(e) t=7.2

(f) t=9.0
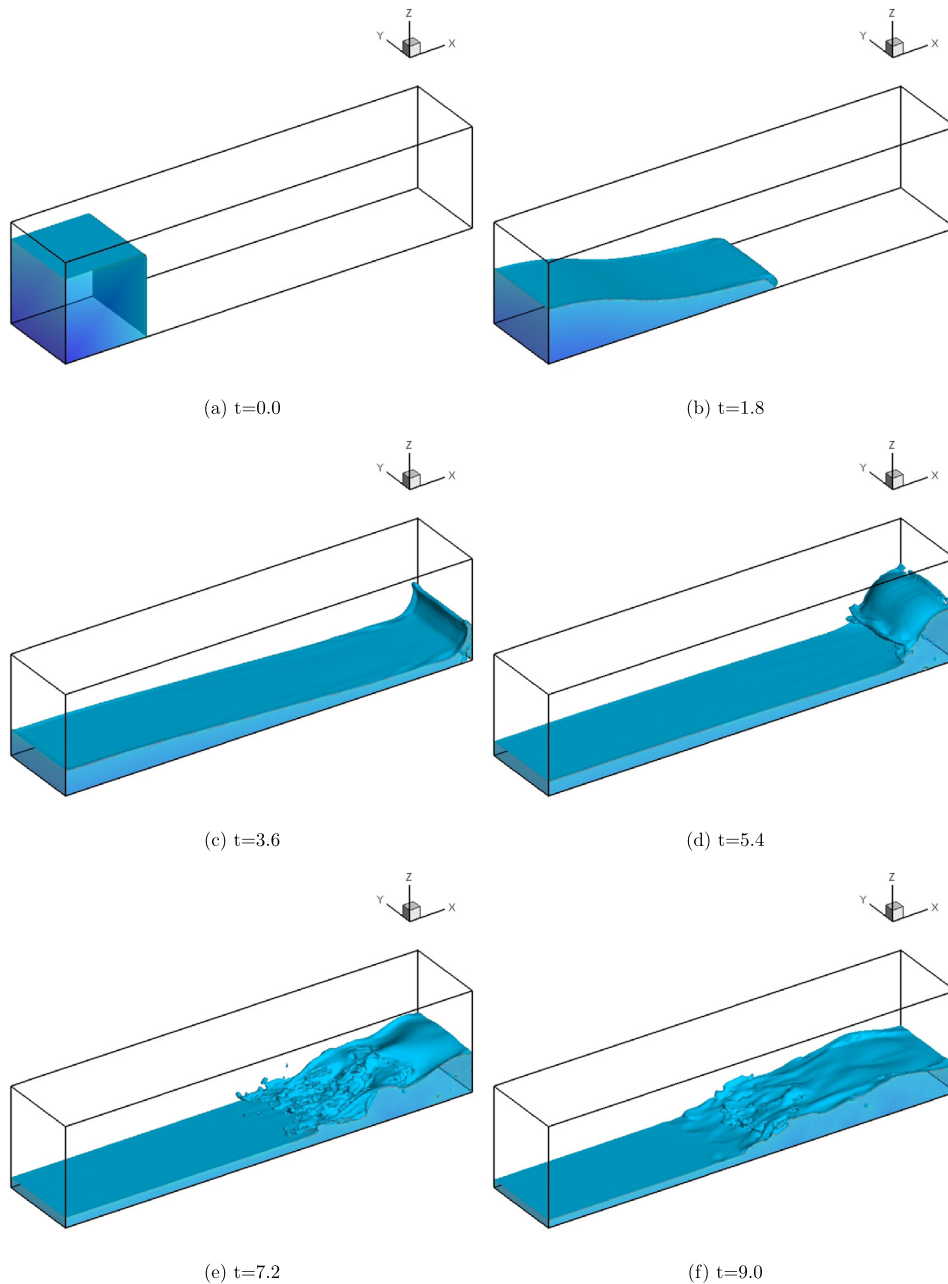
Fig. 10. Numerical results of dam-break flow with dry bed for case A solved by DRP-CRWENO4 scheme at unit grid 50.

5.1. Dam-break flow

Dam-break problems are investigated intensively, and their variations are analyzed [6,51–53]. A water column of length a, width a, and height a is specified in a rectangular domain of size $5a \times 1.25a \times a$. This water column collapses suddenly over a horizontal surface under the action of gravity. We simulate case A for $a = 0.0571$ m and case B for $a = 0.1143$ m.

The effect of grid size on the calculated results is tested by using unit grids of 30, 40, and 50. Instantaneous snapshots of the interface for case A are presented in Fig. 10. A comparison between the experimental and present numerical results for the nondimensional surge front location and water column height is plotted in Fig. 11. As shown in Fig. 11, there is only a small difference between the fine-grid (i.e., unit grid 50) and medium-grid (i.e., unit grid 40) results. The mass losses for the present level set methods using the DRP-CRWENO4 and WENO5 schemes are shown in Fig. 12.
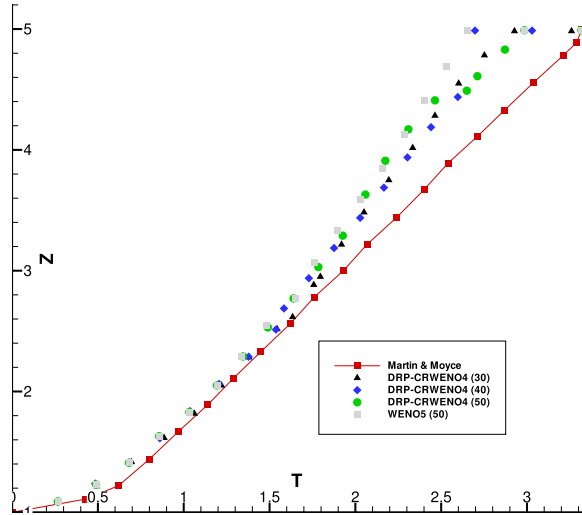
(a) Distance of surge front.
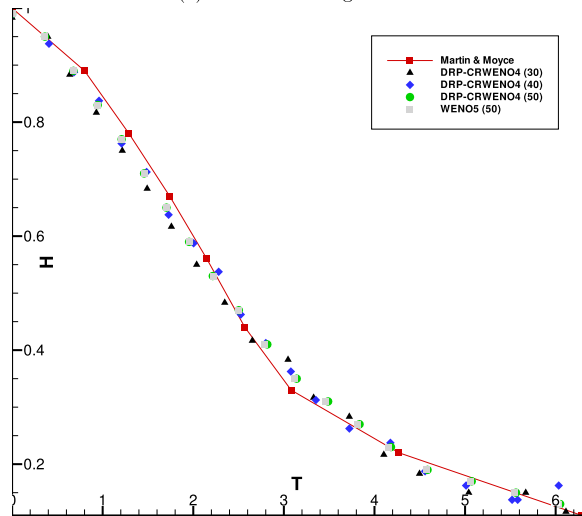
(b) Height of residual column.

Fig. 11. Comparison with experiment [53] for DRP-CRWENO4 scheme at three different unit grids 30,40 and 50.
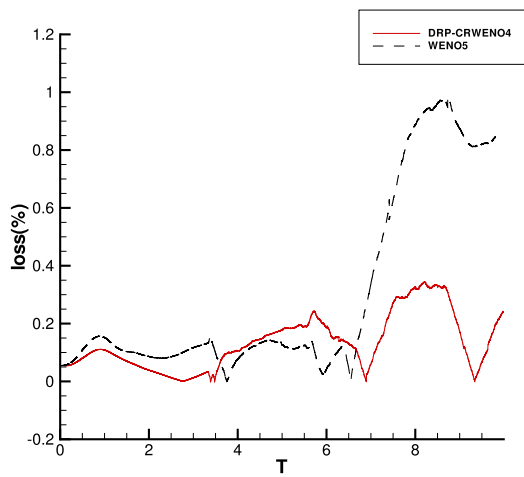
Fig. 12. Mass loss comparison of DRP-CRWENO4 and WENO5 schemes at unit grid 50.

(a) t=0.0

(b) t=1.8

(c) t=3.6

(d) t=5.4

(e) t=7.2

(f) t=9.0
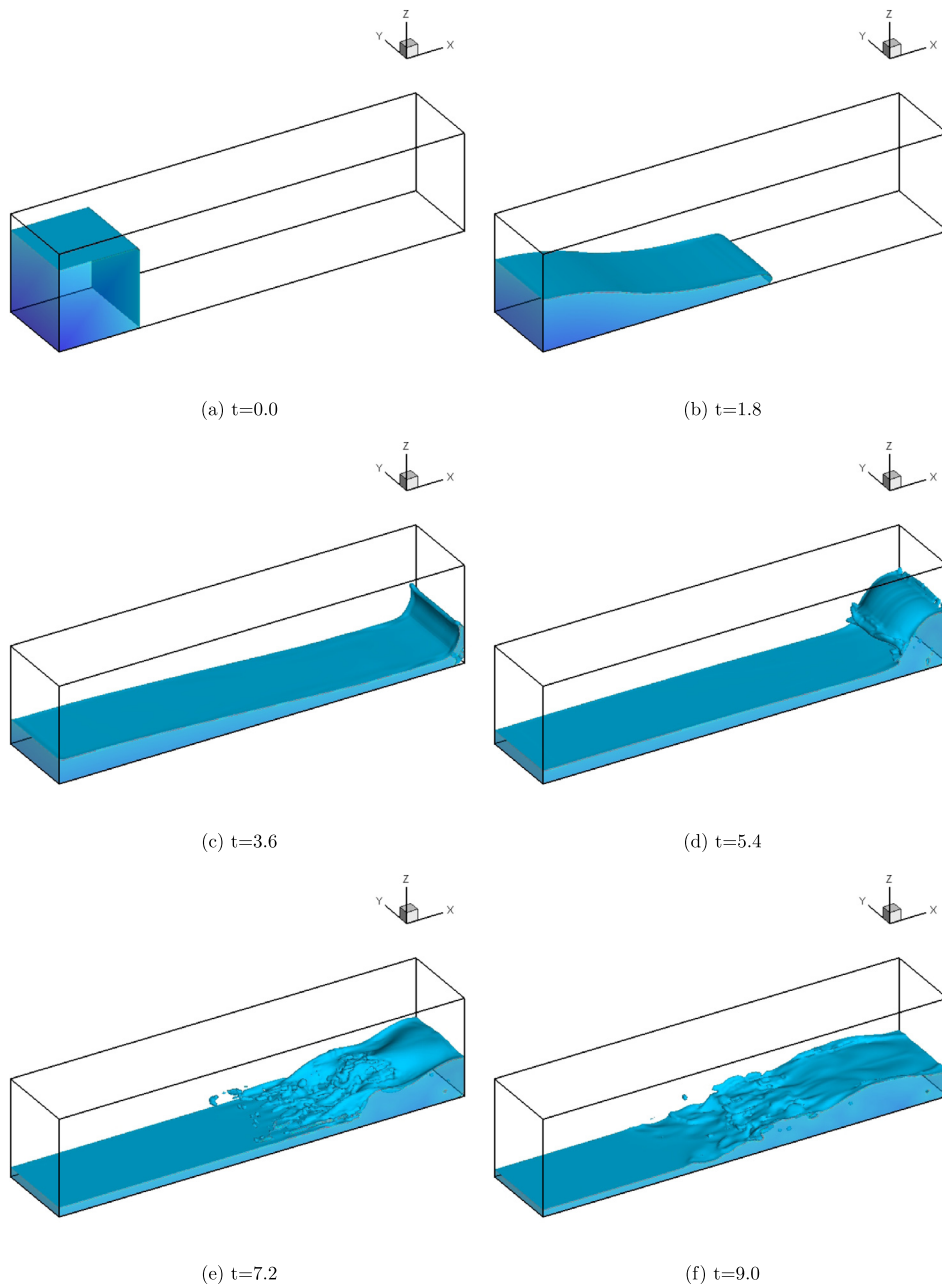
Fig. 13. Numerical results of dam-break flow with dry bed case B solved by DRP-CRWENO4 scheme at unit grid 50.

For case B, the predicted results for the interface in Fig. 13 are shown for the present level set method using the DRP-CRWENO4 scheme. Results are obtained for $t = 1.8$, 3.6, 5.4, 7.2, and 9.0. We see that the dam-break flow hits the vertical right side wall and then begins to rise upward along the right side wall at $t \approx 3.6$. The positions of the surge front location against time are plotted in Fig. 14(a). Good agreement with the experiments of [53] can be observed. In Fig. 14(b), we observe mass losses at approximately $t \approx 10$ for the WENO5 scheme, meaning that nearly 0.9% of the traced mass has been lost because of numerical errors. Additionally, we see in Fig. 14(b) that the mass loss is less than 0.4% for the DRP-CRWENO4 scheme.

5.2. Dam-break flow over a wet bed

The proposed numerical model is tested by simulating the initial stages of dam-break flow over a wet bed. This dam-break flow experiment was conducted by Jánosi et al. [54] in a 10.33 m long, 0.15 m high flume with a flat bed. A vertical
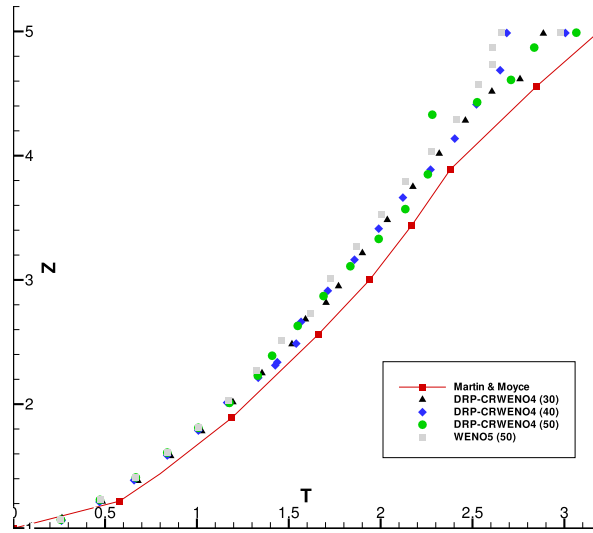
(a) Distance of surge front.
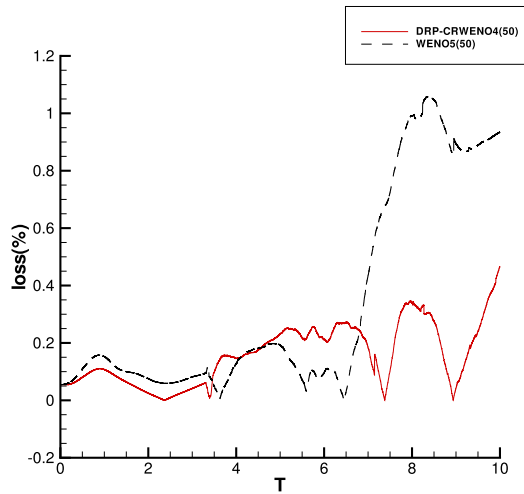
(b) Mass loss evolution.

Fig. 14. (a) Comparison with experiment [53] for distance of surge front at unit grids 30, 40 and 50 of DRP-CRWENO4 scheme. (b) Mass loss evolution of DRP-CRWENO4 and WENO5 schemes at unit grid 50.

baffle plate was located 0.38 m downstream of the upper end, and was used to enclose the water body to a depth 0.15 m upstream. The initial water depth downstream was 0.018 m. The grid with a resolution of $500 \times 50 \times 60$ (unit grid 50) was used in the domain $10 \times 1 \times 1.2$. The velocity components are initially set to zero everywhere, and the pressure distribution is defined to be hydrostatic pressure relative to the top surface of the computational domain. The boundary conditions for the four edges are set at the free slip walls. This study is focused on interface evolution in dam-break wave propagation dynamics. At time $t = 0^+$, the vertical baffle plate is removed suddenly and the water column collapses under the influence of gravity. As shown in Fig. 15(f), the dam-break flow propagating over the wet bed rolls and mixes with the water downstream, entraining the air bubbles at dimensionless time $t = 4.167$. A comparison between experimental [54] and present numerical results is shown in Fig. 16 for the interface evolution at different times. Air entrapment in the experiment behind the surge front from $t = 0.219$ s is completely missing in the current model. To improve the current model, we will try adding some air/bubble models as future work. We also compare this dam-break flow problem using WENO5 scheme with unit grid 60 with experiments in Fig. 17. In Fig. 18, we see that the present results for mass can be preserved well with the DRP-CRWENO4 scheme.

5.3. Dam-break flow caused by partial failure

To validate the developed level set method with the DRP-CRWENO4 scheme, three-dimensional partial dam-break flow is further studied using experiments conducted by Fraccarollo and Toro [55]. Initially, a water column of length 1.0 m, width
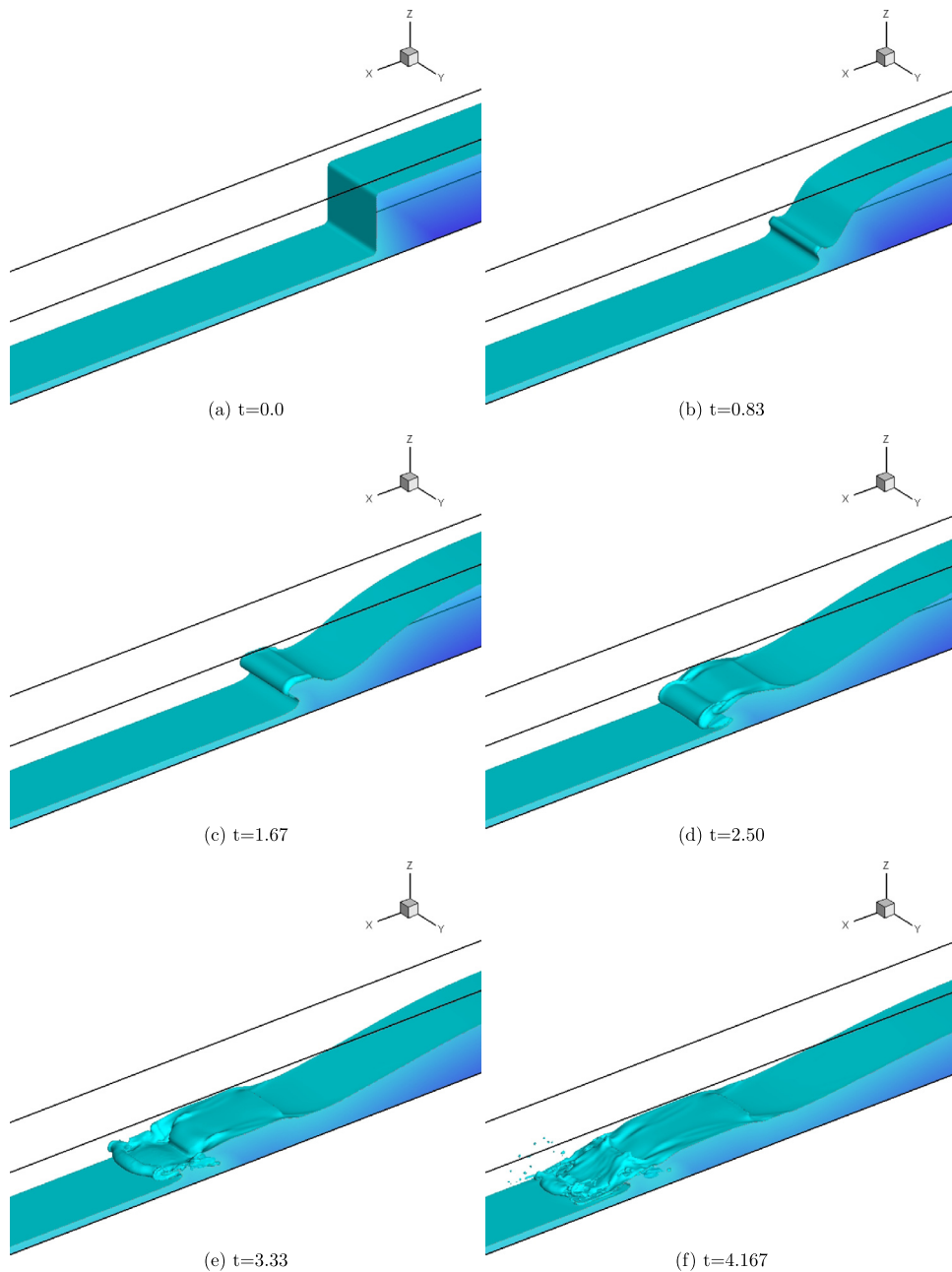
Fig. 15. Numerical results of dam-break flow with wet bed solved by DRP-CRWENO4 scheme at unit grid 50.

2.0 m, and height 0.6 m is placed in the right part of the flume. There is no water in the left part of the flume, as shown in Fig. 19. The time evolution of water height (including gates G5A, GC, and G0, which were placed inside the reservoir) has been calculated. Fig. 20 shows the predicted free surface profiles. The simulation of this three-dimensional dam-break flow problem has been investigated with $150 \times 100 \times 35$ grids (unit grid 50). Fig. 21(a)–(c) compares the numerical and measured values for water height at gates G5A, GC, and G0 over time, respectively. As expected, a good correlation is observed between the numerical results and experimentally measured results in [55]. Mass conservation results are shown in Fig. 21(d).

5.4. Dam-break flow over a rectangular obstacle

A study of three-dimensional dam-break flow over a rectangular obstacle was carried out at the Maritime Research Institute of the Netherlands (MARIN) [56]. This study is considered to validate the present model developed using the
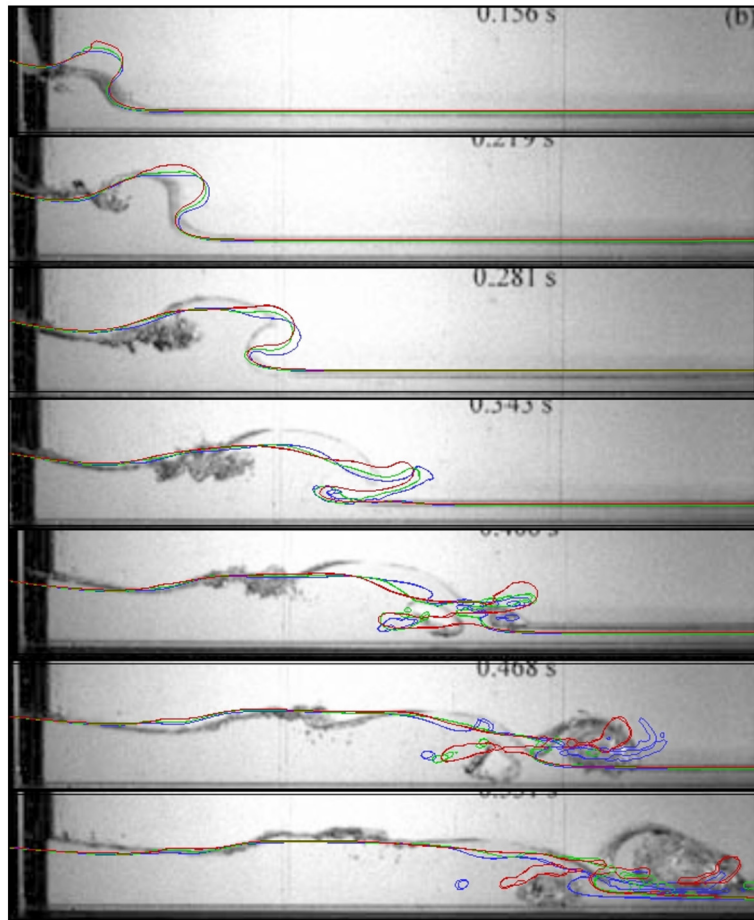
Fig. 16. Comparison to experiments [54] for present two-phase flow model at three unit grid, 40, 50 and 60 in three different colors, red, green and blue, respectively. (For interpretation of the colors in the figure(s), the reader is referred to the web version of this article.)

proposed interface-preserving level set method with the DPP-CRWENO4 scheme. The computational domain 3.2 m × 1 m × 1 m is considered. As shown in Fig. 22, the initial water column inside the reservoir was 0.55 m in height. It collapses under the action of gravity and then impacts a stationary object. This stationary object with the size of 0.4 m × 0.16 m × 0.16 m is located downstream of the reservoir. Four water-level heights ($H1$–$H4$) were installed: one in the reservoir and three in the tank [21,56,57]. A grid of $192 \times 60 \times 60$ has been used for this simulation.

Several snapshots of the evolution of the free surface are shown in Fig. 23(a)–(d) at $t = 1.33$, 2.67, 4.00, and 6.67, respectively. In Fig. 24, the time history of predicted water heights is shown at four locations ($H1$–$H4$). Good agreement can be seen between the predicted water heights of the simulation and experiment. In Fig. 25, mass conservation results for the DRP-CRWENO4 and WENO5 schemes are calculated. The mass loss does not exceed 0.1% for the DRP-CRWENO4 scheme, and is approximately 2.2% for the WENO5 scheme.

6. Concluding remarks

A two-phase flow algorithm based on the interface-preserving level set method was developed for three-dimensional dam-break flows on uniform staggered Cartesian grids. The interface (zero-level set) was captured implicitly by solving the level set evolution equation. We compared numerical schemes for the advection of the level set function, including the WENO5 scheme and the proposed DRP-CRWENO4 scheme. DRP-CRWENO4, which used a compact stencil, yielded a higher-order accuracy, lower truncation errors, and less dispersion errors. A non-oscillatory limiter was also introduced for the DRP-CRWENO4 scheme to avoid oscillations across discontinuities. The WENO5 and DRP-CRWENO4 schemes were verified with benchmark cases: wave propagation, rotating slotted disk, and vortex deformation problems. For both smooth and discontinuous solutions, the DRP-CRWENO4 scheme was shown to be superior to the WENO5 scheme. Mass loss from numerical dissipation on thin filaments and the disk corner was reduced for the Zalesak's disk and the vortex deforming problems, respectively, by using the WENO5 scheme. Comparison between the hybrid particle level set method and the pro-
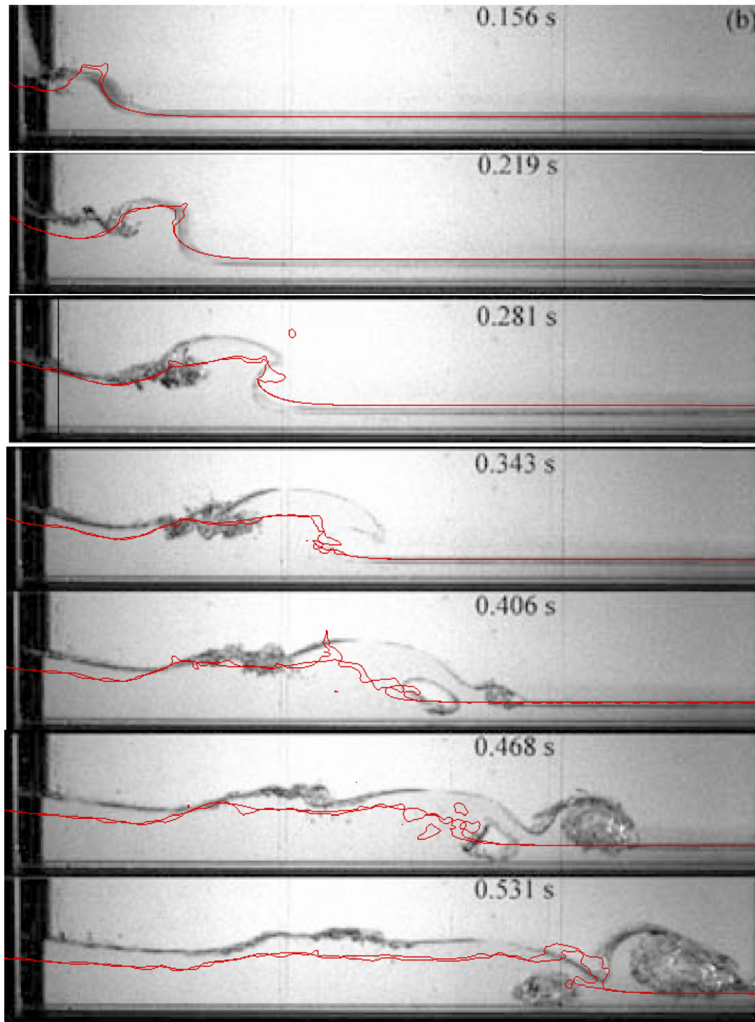
Fig. 17. Comparison with experiments of dam-break problem flow over a wet bed using WENO5 scheme with unit grid 60.
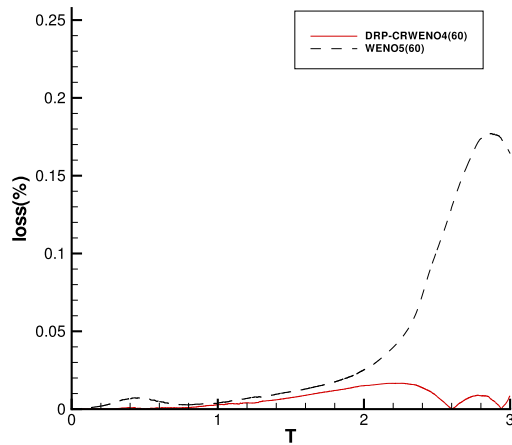

Fig. 18. Comparison of mass loss evolution for DRP-CRWENO4 and WENO5 schemes at unit grid 60.
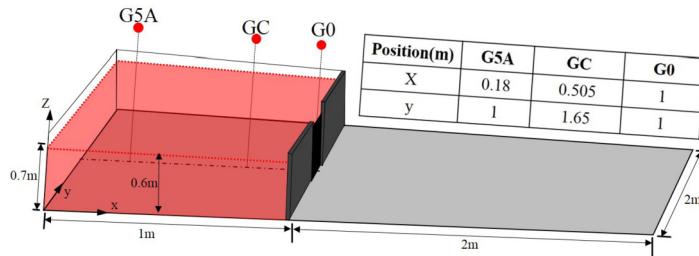
Fig. 19. Schematic of the initial condition for dam-break flow caused by partial failure problem.
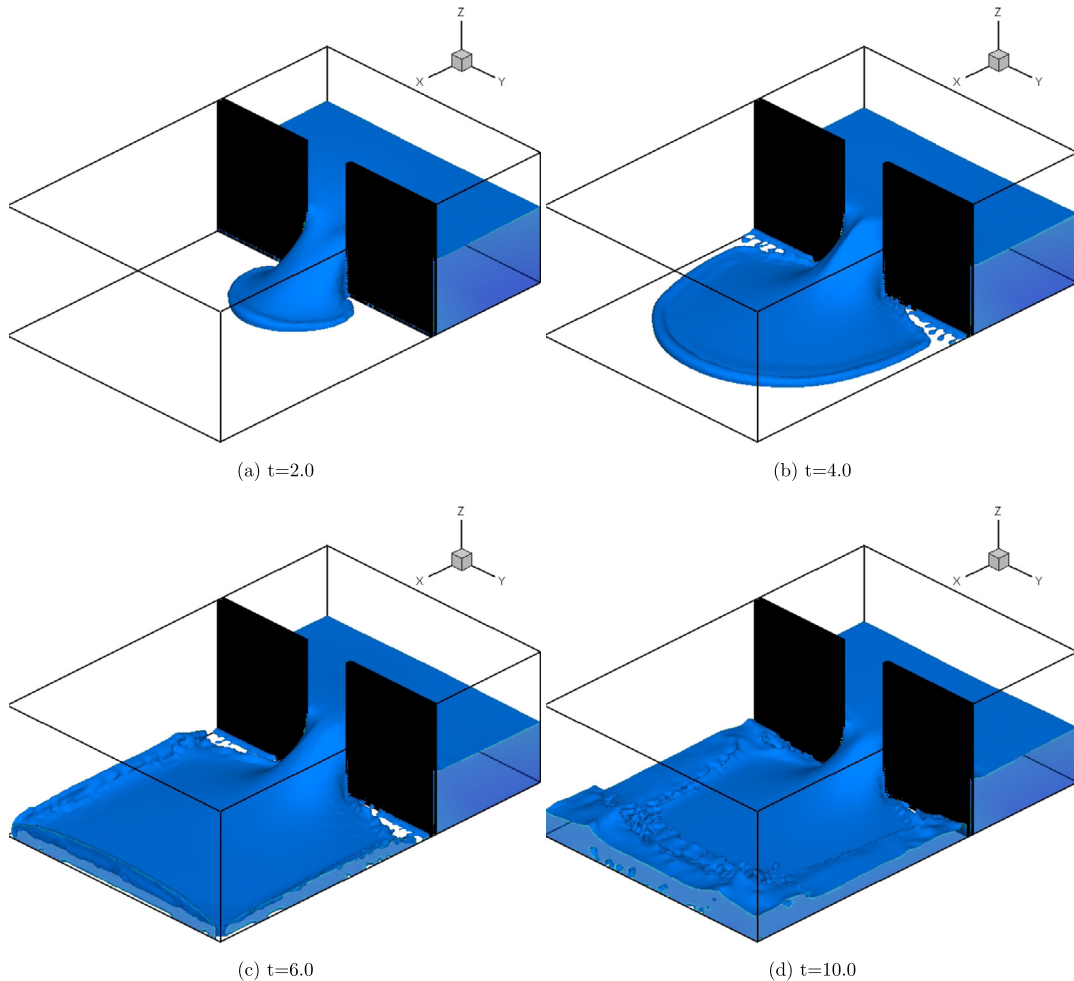

(a) t=2.0

(b) t=4.0

(c) t=6.0

(d) t=10.0

Fig. 20. Numerical results of dam-break flow of partial failure solved by DRP-CRWENO4 scheme at unit grid 50.

posed level set method in mass conservation shows that both methods perform quite well in solving the vortex deforming, Zalesak's disk and sphere problems.

For complex dam-break flows over a dry bed, the surge front location and the water column height showed good agreement with the experimental data obtained by Martin and Moyce [53]. For complex dam-break flows over a wet bed, the proposed numerical method was demonstrated to successfully predict the evolution of an interface; the results were in good agreement with the numerical results of Jánosi et al. [54]. For dam-break flow over both dry and wet beds, mass loss was greatly reduced by using the proposed DRP-CRWENO4 scheme rather than the WENO5 scheme. Dam-break flow caused by partial failure was also numerically investigated. The predicted results for water height agreed well with the experimental results introduced in [55]. Finally, the implementation of the current level set model was evaluated for a problem involving
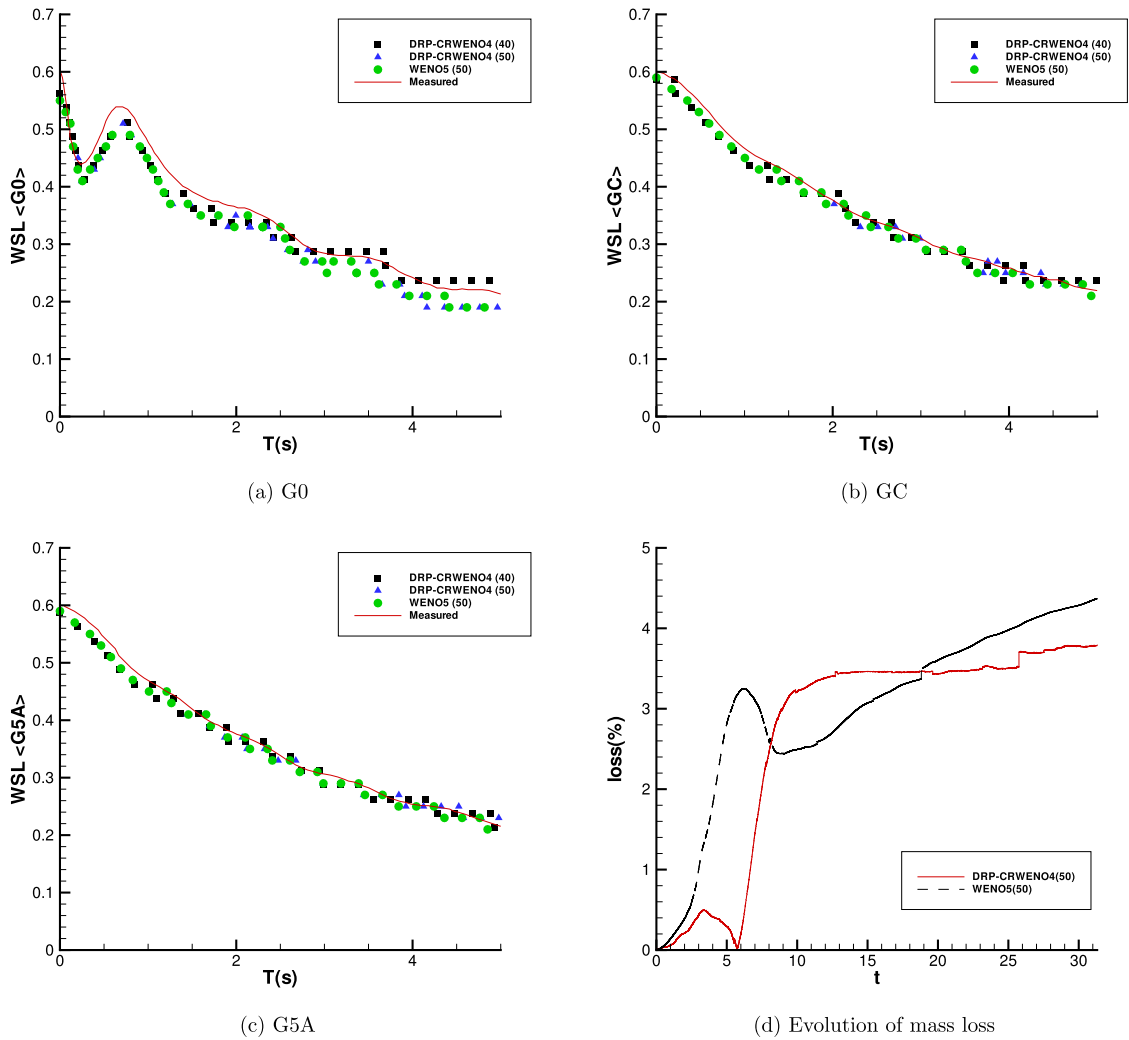
(a) G0

(b) GC

(c) G5A

(d) Evolution of mass loss

Fig. 21. (a), (b), (c) Water levels at three distinct places, denoted by G0, GC and G5A. Comparison between numerical results solved by DRP-CRWENO4 scheme and measured data [55]. The result is carried out at unit grid 40 and 50. (d) Case of dam-break flow with partial failure. Comparison of mass loss evolution for DRP-CRWENO4 and WENO5 at unit grid 50.
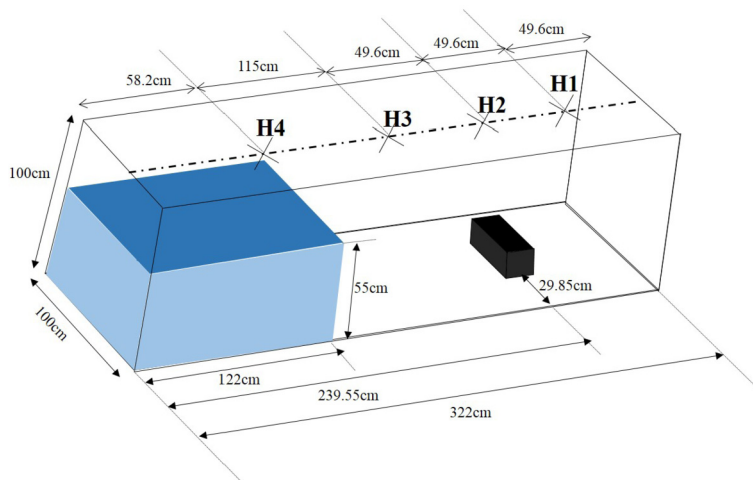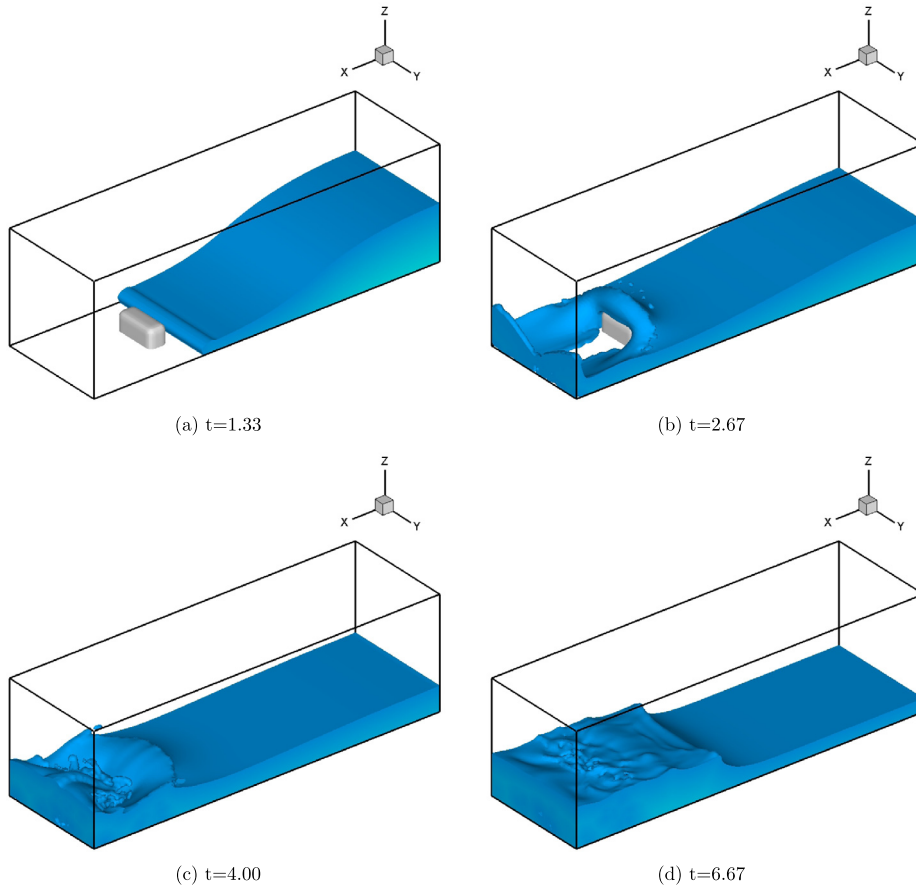

Fig. 22. Schematic of the initial condition for dam-break flow over a rectangular obstacle.

(a) t=1.33

(b) t=2.67

(c) t=4.00

(d) t=6.67

Fig. 23. Numerical results of dam-break flow with an obstacle solved by DRP-CRWENO4 scheme at unit grid 60.

dam-break flow over an obstacle. The numerical results indicate that the proposed DRP-CRWENO4 scheme is accurate in the presence of complex three-dimensional dam-break flow phenomena.

Acknowledgements

Appendix A

Calculation for the coefficients in equation (27)

Subtract Eq. (28) from Eq. (27) and divide the resulting equation by Δx, and we can obtain

$$\widetilde{A}(\frac{\hat{F}_{i-\frac{1}{2}} - \hat{F}_{i-\frac{3}{2}}}{\Delta x}) + (\frac{\hat{F}_{i+\frac{1}{2}} - \hat{F}_{i-\frac{1}{2}}}{\Delta x}) + \widetilde{C}(\frac{\hat{F}_{i+\frac{3}{2}} - \hat{F}_{i+\frac{1}{2}}}{\Delta x})$$
$$= \widetilde{a}(\frac{F_{i-1} - F_{i-2}}{\Delta x}) + \widetilde{b}(\frac{F_i - F_{i-1}}{\Delta x}) + \widetilde{c}(\frac{F_{i+1} - F_i}{\Delta x}). \tag{78}$$

According to the definition of $\frac{\partial F}{\partial x}|_{i-1} = \frac{\hat{F}_{i-\frac{1}{2}} - \hat{F}_{i-\frac{3}{2}}}{\Delta x}$, $\frac{\partial F}{\partial x}|_i = \frac{\hat{F}_{i+\frac{1}{2}} - \hat{F}_{i-\frac{1}{2}}}{\Delta x}$ and $\frac{\partial F}{\partial x}|_{i+1} = \frac{\hat{F}_{i+\frac{3}{2}} - \hat{F}_{i+\frac{1}{2}}}{\Delta x}$, and substitute these definitions into Eq. (78), Eq. (78) can be rewritten as
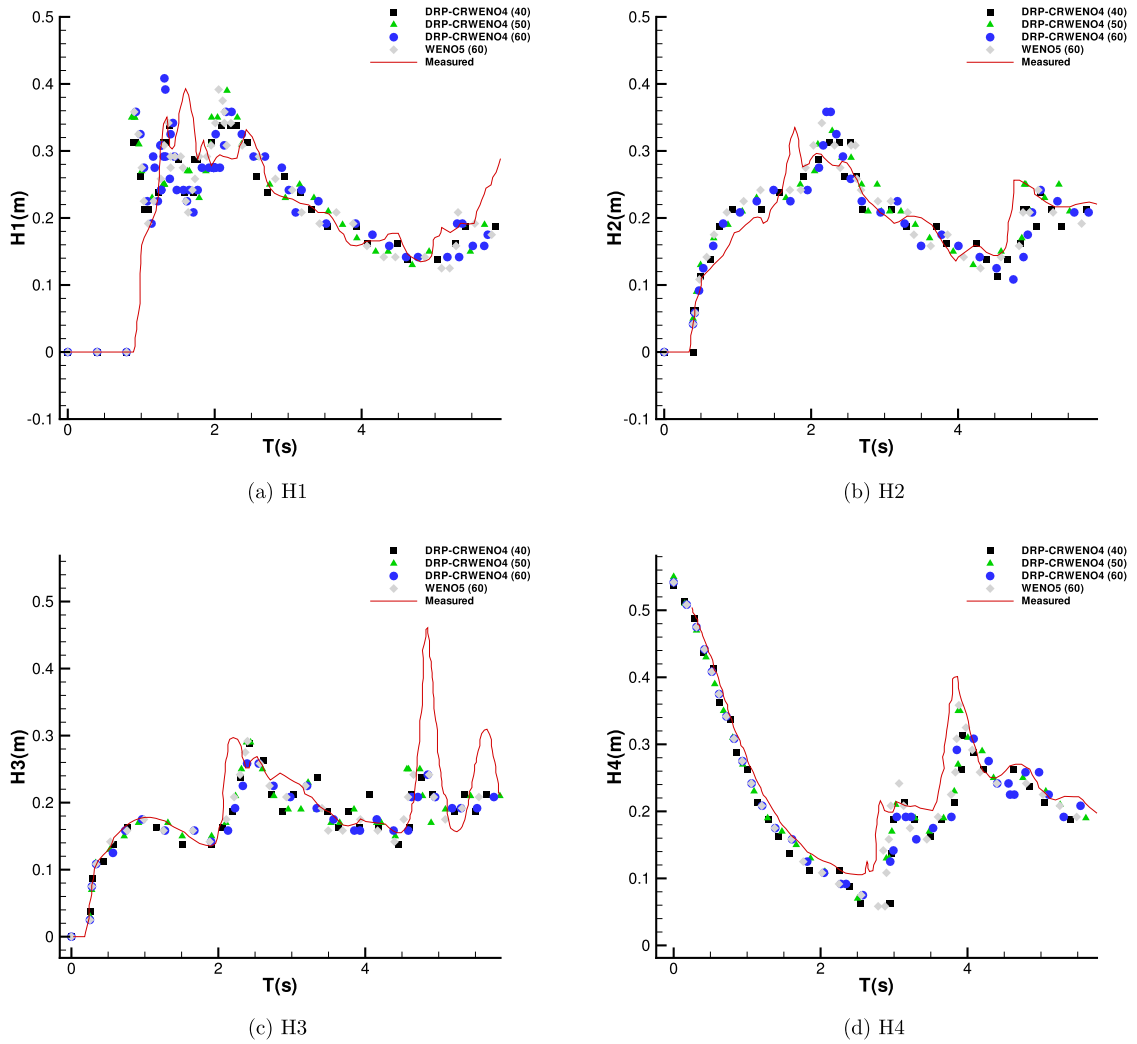
Fig. 24. Water levels at four distinct places for the dam-break flow with obstacle, comparison between numerical result and measured data [56]. The result is carried out by DRP-CRWENO4 scheme at unit grids 50 and 60.
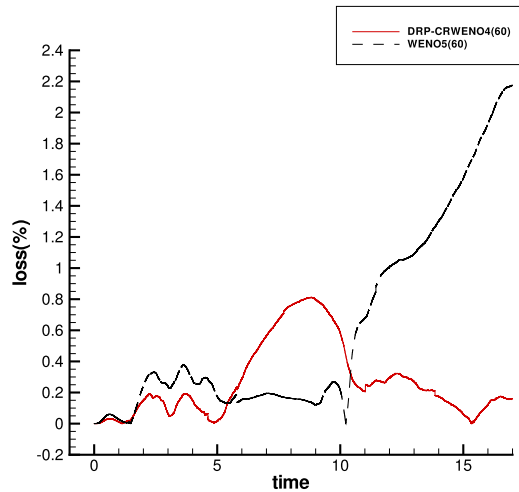

Fig. 25. Case of dam-break flow with obstacle. Comparison of mass loss evolution for DRP-CRWENO4 and WENO5 schemes at unit grid 60.

$$\widetilde{A}(\frac{\partial F}{\partial x}|_{i-1}) + \frac{\partial F}{\partial x}|_i + \widetilde{C}(\frac{\partial F}{\partial x}|_{i+1})$$

$$= \frac{-\widetilde{a}F_{i-2} + (\widetilde{a} - \widetilde{b})F_{i-1} + (\widetilde{b} - \widetilde{c})F_i + \widetilde{c}F_{i+1}}{\Delta x}. \tag{79}$$

Compare the coefficients in Eq. (79) and the optimized coefficients in Eq. (14) derived in section 3.1.1.1, we can obtain the unknown coefficients in Eq. (27) as $\widetilde{A} = 0.5418416108$, $\widetilde{C} = 0.1527194630$, $\widetilde{a} = 0.0648536914$, $\widetilde{b} = 1.106695303$, and $\widetilde{c} = 0.5230120803$.

References

[1] R. Marsooli, W. Wu, 3-d finite-volume model of dam-break flow over uneven beds based on VOF method, Adv. Water Resour. 70 (2014) 104–117.
[2] S.L. Lee, S.R. Sheu, A new numerical formulation for incompressible viscous free surface flow without smearing the free surface, Int. J. Heat Mass Transf. 44 (10) (2001) 1837–1848.
[3] M. Aanjaneya, S. Patkar, R. Fedkiw, A monolithic mass tracking formulation for bubbles in incompressible flow, J. Comput. Phys. 247 (2013) 17–61.
[4] S. Osher, R. Fedkiw, Level Set Methods and Dynamic Implicit Surfaces, Appl. Math. Sci., vol. 153, Springer-Verlag, New York, 2003.
[5] S. Osher, R. Fedkiw, Level set methods: an overview and some recent results, J. Comput. Phys. 169 (2) (2001) 463–502.
[6] A. Yang, S. Chen, Y. Liu, X. Yang, An upwind finite volume method for incompressible inviscid free surface flows, Comput. Fluids 101 (2014) 170–182.
[7] C. Yang, Z.S. Mao, Numerical simulation of inter phase mass transfer with the level set approach, Chem. Eng. Sci. 60 (2005) 2643–2660.
[8] B. Zhu, X. Zhang, N. Wang, S. Fatikow, Optimize heat conduction problem using level set method with a weighting based velocity constructing scheme, Int. J. Heat Mass Transf. 99 (2016) 441–451.
[9] M. Choi, G. Son, W. Shim, A level-set method for droplet impact and penetration into a porous medium, Comput. Fluids 145 (2) (2017) 153–166.
[10] L.C. Ngo, H.G. Choi, Efficient direct re-initialization approach of a level set method for unstructured meshes, Comput. Fluids 154 (1) (2017) 167–183.
[11] M.H. Chung, An adaptive Cartesian cut-cell/level-set method to simulate incompressible two-phase flows with embedded moving solid boundaries, Comput. Fluids 71 (2013) 469–486.
[12] H. Kim, M. Liou, Accurate adaptive level set method and sharpening technique for three dimensional deforming interfaces, Comput. Fluids 44 (1) (2011) 111–129.
[13] K. Luo, C.X. Shao, Y. Yang, J.R. Fan, A mass conserving level set method for detailed numerical simulation of liquid atomization, J. Eng. Thermophys.-Rus. 298 (2015) 495–519.
[14] R.R. Nourgaliev, S. Wiri, T.N. Dinh, On improving mass conservation of level set by reducing spatial discretization errors, Int. J. Multiph. Flow 31 (12) (2005) 1329–1336.
[15] M. Hermann, Refined Level Set Grid Method for Tracking Interfaces, Annual Research Briefs, 2014, pp. 3–18.
[16] A. Salih, S.G. Moulic, Some numerical studies of interface advection properties of level set method, Sadhana 34 (2) (2009) 271–298.
[17] M. Sussman, E. Fatemi, An efficient, interface-preserving level set redistancing algorithm and its application to interfacial incompressible fluid flow, SIAM J. Sci. Comput. 20 (4) (1999) 1165–1191.
[18] M.J. Ni, S. Komori, N.B. Morley, Direct simulation of falling droplet in a closed channel, Int. J. Heat Mass Transf. 49 (1–2) (2006) 366–376.
[19] Y.C. Chang, T.Y. Hou, B. Merriman, S. Osher, A level set formulation of Eulerian interface capturing methods for incompressible fluid flows, J. Comput. Phys. 124 (124) (1996) 449–464.
[20] E. Olsson, G. Kreiss, A conservative level set method for two phase flow, J. Comput. Phys. 210 (1) (2005) 225–246.
[21] C.E. Kees, I. Akkerman, M.W. Farthing, Y. Bazilevs, A conservative level set method suitable for variable-order approximations and unstructured meshes, J. Comput. Phys. 230 (12) (2011) 4536–4558.
[22] L. Zhao, J. Mao, X. Bai, X. Liu, J.J.R. Williams, Finite element implementation of an improved conservative level set method for two-phase flow, Comput. Fluids 100 (1) (2014) 138–154.
[23] R.F. Ausas, E.A. Dari, G.C. Buscaglia, A geometric mass-preserving redistancing scheme for the level set function, Int. J. Numer. Methods Fluids 65 (8) (2011) 989–1010.
[24] Y. Sun, C. Beckermann, Sharp interface tracking using the phase-field equation, J. Comput. Phys. 220 (2) (2007) 626–653.
[25] G. Son, Efficient implementation of a coupled level-set and volume-of-fluid method for three dimensional incompressible two-phase flows, Numer. Heat., Part B, Fundam. 43 (6) (2003) 549–565.
[26] I. Chakraborty, G. Biswas, P.S. Ghoshdastidar, A coupled level-set and volume-of-fluid method for the buoyant rise of gas bubbles in liquids, Int. J. Heat Mass Transf. 58 (1–2) (2013) 240–259.
[27] B.M. Ningegowda, B. Premachandran, A coupled level set and volume of fluid method with multi-directional advection algorithms for two-phase flows with and without phase change, Int. J. Heat Mass Transf. 79 (2014) 532–550.
[28] Z. Wang, J. Yang, F. Stern, A new volume-of-fluid method with a constructed distance function on general structured grids, J. Comput. Phys. 231 (9) (2012) 3703–3722.
[29] Z. Wang, A.Y. Tong, A sharp surface tension modeling method for two-phase incompressible interfacial flows, Int. J. Numer. Methods Fluids 64 (7) (2010) 709–732.
[30] N. Balcázar, O. Lehmkuhl, L. Jofre, J. Rigola, A. Oliva, A coupled volume-of-fluid/level-set method for simulation of two-phase flows on unstructured meshes, Comput. Fluids 124 (2) (2016) 12–29.
[31] D.L. Sun, W.Q. Tao, A coupled volume-of-fluid and level set (VOSET) method for computing incompressible two-phase flows, Int. J. Heat Mass Transf. 53 (4) (2010) 645–655.
[32] T. Wang, H. Li, Y. Feng, D. Shi, A coupled volume-of-fluid and level set (VOSET) method on dynamically adaptive quadtree grids, Int. J. Heat Mass Transf. 67 (4) (2013) 70–73.
[33] K. Ling, Z.H. Li, D.L. Sun, Y.L. He, W.Q. Tao, A three-dimensional volume of fluid & level set (VOSET) method for incompressible two-phase flow, Comput. Fluids 118 (2015) 293–304.
[34] Z.Z. Cao, D.L. Sun, B. Yu, J.J. Wei, A coupled volume-of-fluid and level set (VOSET) method based on remapping algorithm for unstructured triangular grids, Int. J. Heat Mass Transf. 111 (2017) 232–245.
[35] S.P. van der Pijl, A. Segal, C. Vuik, P. Wesseling, A mass-conserving level-set method for modeling of multi-phase flows, Int. J. Numer. Methods Fluids 47 (4) (2005) 339–361.
[36] S.P. van der Pijl, A. Segal, C. Vuik, P. Wesseling, Computing three-dimensional two-phase flows with a mass-conserving level set method, Comput. Vis. Sci. 11 (4) (2008) 221–235.
[37] D. Enright, R. Fedkiw, J. Ferziger, I. Mitchell, A hybrid particle level set method for improved interface capturing, J. Comput. Phys. 183 (1) (2002) 83–116.

[38] Philip J. Archer, W. Bai, A new non-overlapping concept to improve the hybrid particle level set method in multi-phase fluid flows, J. Comput. Phys. 282 (2015) 317–333.
[39] D. Gaudlitz, N.A. Adams, On improving mass-conservation properties of the hybrid particle level set method, Comput. Fluids 37 (2008) 1320–1331.
[40] Z. Wang, J. Yang, F. Stern, An improved particle correction procedure for the particle level set method, J. Comput. Phys. 228 (2009) 5819–5837.
[41] J. Liang, L. Fengbin, C. Darong, A fast particle level set method with optimized particle correction procedure for interface capturing, J. Comput. Phys. 299 (2015) 804–819.
[42] M. Sussman, P. Smereka, S. Osher, A level set approach for computing solutions to incompressible two-phase flow, J. Comput. Phys. 114 (1) (1994) 146–159.
[43] R. Fedkiw, T. Aslam, B. Merriman, S. Osher, A non-oscillatory Eulerian approach to interfaces in multimaterial flows (the ghost fluid method), J. Comput. Phys. 152 (1999) 457–492.
[44] G.S. Jiang, C.W. Shu, Efficient implementation of weighted ENO schemes, J. Comput. Phys. 126 (1) (1996) 202–228.
[45] S.K. Lele, Compact finite difference schemes with spectral-like resolution, J. Comput. Phys. 103 (1) (1992) 16–42.
[46] C.K.W. Tam, J.C. Webb, Dispersion-relation-preserving finite difference schemes for computational acoustics, J. Comput. Phys. 107 (2) (1993) 262–281.
[47] B. Zhao, Z. Tian, High-resolution high-order upwind compact scheme-based numerical computation of natural convection flows in a square cavity, Int. J. Heat Mass Transf. 98 (2016) 313–328.
[48] D. Ghosh, J.D. Baeder, Compact reconstruction schemes with weighted ENO limiting for hyperbolic conservation laws, SIAM J. Sci. Comput. 34 (3) (2012) A1678-A1706.
[49] G.S. Jiang, D. Peng, Weighted ENO schemes for Hamilton-Jacobi equations, SIAM J. Sci. Comput. 21 (6) (2000) 2126–2143.
[50] C.W. Shu, Total-variation diminishing time discretizations, SIAM J. Sci. Stat. Comput. 9 (6) (1988) 1073–1084.
[51] P.H. Chiu, Y.T. Lin, A conservative phase field method for solving incompressible two-phase flows, J. Comput. Phys. 230 (1) (2011) 185–204.
[52] C. Hu, M. Sueyoshi, Numerical simulation and experiment on dam break problem, J. Mar. Sci. Appl. 9 (2) (2010) 109–114.
[53] J.C. Martin, W.J. Moyce, An experimental study of collapse of liquid columns on a rigid horizontal plane, Philos. Trans. R. Soc. Lond. Ser. A 244 (882) (1952) 312–324.
[54] I.M. Jánosi, D. Jan, K.G. Szabó, T. Tél, Turbulent drag reduction in dam-break flows, Exp. Fluids 37 (2) (2004) 219–229.
[55] L. Fraccarollo, E.F. Toro, Experimental and numerical assessment of the shallow water model for two-dimensional dam-break type problems, J. Hydraul. Res. 33 (6) (1995) 843–864.
[56] K.M.T. Kleefsman, G. Fekken, A.E.P. Veldman, B. Iwanowski, B. Buchner, A volume-of-fluid based simulation method for wave impact problems, J. Comput. Phys. 206 (1) (2005) 363–393.
[57] X. Lv, Q.P. Zou, D.E. Reeve, Y. Zhao, A preconditioned implicit free-surface capture scheme for large density ratio on tetrahedral grids, Commun. Comput. Phys. 11 (1) (2012) 215–248.